KINEMATICS AND DYNAMICS OF THE SONAWANI (BALAGHAT) TECTONIC NAPPES

Dr. N.L. Dongre.

"A life too full of excitement is an exhausting life, in which continually stronger stimuli are needed to give the thrill that has come to be thought an essential part of pleasure."

— Bertrand Russell

The Sonawani fold contains early Dharwar Group rocks and basement inliers. The geology is shown to be deformed by large-scale, west-vergent and north facing early Palaeozoic folds that represent D_2 with in the Nappe. Subsequent D_3 deforming led to refolding or tightening of F_2 folds, so that the Sonawani Anti-form is, in essence, a composit F_2/F_3 fold. F_2 and F_3 folds refold a regional scale, originally recumbent, isoclinals F_1 fold Nappe of 1,340 million years age. The Nappe is cored by thin sliver of basement, gneiss; the lower limb comprises magmatic rocks, exposed in the window. The upper limb of the fold occupies most of metamorphic rocks and is stratigraphhically coherent and right-way up. Within this sequence, the upper and lower Sonawani psammite is barely deformed, preserving trough cross-bedding and large-scale channels in thick beds.

ABSTRACT: *Two-dimensional numerical simulations of lithospheric shortening with a crust containing weak and strong inclusions are present here. Thermo-mechanical coupling is consisted here and a crustal-scale shear zone develops self-consistently due to viscous heating and thermal softening of temperature dependent viscosities. Various tests for crustal conditions are done showing that 1) the thickness of and strain rates within the shear zone are independent on the numerical resolution and applied numerical method (finite element and finite difference method), 2) the shear zone is stable and rotates during large strain deformation, 3) the numerical algorithm conserves total thermal and mechanical energies, and 4) the bulk horizontal force balance is fulfilled during large strain deformation. The fold Nappe develops around the shear zone in the lithospheric shortening simulation. The stresses in the crust are limited in this simulation by a friction angle of 30°. A major tectonic overpressure (P_O) happens in strong lower crustal rocks and in strong inclusions. Significant P_O also occurs in a weak inclusion that is only partly surrounded by strong crustal rock directing that a continuous*

strong "vessel" is not necessary to generate significant P_O in weak rocks. Maximal values of P_O are ~2.2 GPa with corresponding deviatoric stresses ~1.5 GPa and occur in a depth of ~42 km. Maximal pressure of ~ 3.4 GPa and maximal temperatures > 700 °C happen during the formation of the Sonawani fold Nappe in crustal depth. Synthetic pressure-temperature paths exhibit entire cycles of pressure and temperature increase and decrease, and propose that crustal rocks in depths < 50 km can reach the ultrahigh pressure metamorphic facies fields. Applications to tectonic Nappes with high and ultra-high pressure rocks in the Sonawani are discussed, and a dynamic model for the evolution of fold Nappes in the Sonawani is proposed.

1. Introduction

A number of mountain belts on earth result from superimposed orogenies. The reason to treat the Sonawani Nappes is contribution to the earth science of Balaghat, India. The great Geologist Burton (1912) had traced the Sonawani Nappe and given a geological name after the village Sonawani (21° 55' 7. 88" N 79°52'7.97" E). This is a sincere efforts and my strategy is to unravel aspects of orogenies of the Sonawani Nappe formation. It is established cross cutting relationships of different metamorphic rocks and associated dikes with tectono metamorphic fabrics in the field. The Sonawani Nappe (Fig.1 A) is occupied an area to the north-west of the Wainganga River valley in the Balaghat District of India. The Nappe extends across the Sonawani forest north of Ramrama over an exposer about 15 kilometres, the width of the belt is about 8 kilometres. It gets under alluvial cover of both the east and the west only the southern margin of the thrust, where dip appears to be moderate angles of 30° - 40° to the north. The Sonwani is the name of phyllites schists and calc silicate rocks of the area, which were unconformable below the Chilpi-Ghat series further east (Burton 1912). Fermer (1936) distinguished two horizons of manganese –rocks at the base of the Chilpi Ghat series and at the base of the Sonawani series. These rocks were intensely folded and metamorphosed. Burton was very much clear that Archaen sedimentaries are into the Chilpi Ghat series and the Sonawani. This paper embodies the geology of the country around the Sonawani near Waraseoni (21.7647° N, 80.0494° E). The structure of the Nappe has been studied in detail and the rocks which are of Lower Dharwar age are distinguished stratigraphically to belong to the older Sonawani series and the younger Chilpi Ghat series. The large recumbent fold is an undulation in the stratified rocks of the earth's crust having an essential horizontal axil plane; both processes position the Sonawani older rocks over younger Chilpi Ghat rocks. In places, erosion cut into the sonawani neppe so deeply that circular or elliptical patch of the younger Chilpi Ghat series and sedimentary and crush-conglomerates bounding the south-eastern margin of the Chilpi outcrop in this region. The Chilpi Ghat series is exposed and completely surrounded by the Sonawani series. The Sonawani is structurally very complex and it forms an arc, broadly convex to the south. Mostly the Sonawani series is overlain by the Chilpi-Ghat series which is made up of trap rocks, grits, conglomarates, green stones etc. The general strike of the rocks is N.E.S.W in the east, E.W. in the middle and W.N.N-E.S.W in the west. The southern part of the belt constitute a zone of isoclinals fold with steep (50°-80°) dips to the north; in the middle strip the fold are recumbent, with 30° to 60° dip to south; the northern strip shows thrust sheets-Nappe. The large body or sheet of the Sonawani rocks that has been moved a distance of about 15 kilometers from its original position of faulting and folding. In the east, the folds lean to the south with the axial plan dipping to the north of law angle of 10° to 30°. There is numerous steep dipping strike-faults in the different parts of the belt and they are generally thrust faults. The faults as well as the thrust faults tend to be arranged *enechelon,* these being shifted progressively to north as proceeded east or west from central region. The fold axes plunge to the N.E. The main folds have been cross folded at a later date, the cores of the cross folds being often occupied by granite of post folding age. The axes of the cross folds plunge at low angles to the west or south west. The Sonawani Nappe has low southern dip, the dip increasing gradually southwards. The Sonawani is a member of Sausar Group. The Sonawani contain calarous rocks, quartsmucovite schists and granulites. The grade of metamorphism increases gradually westwards and northwards. Near
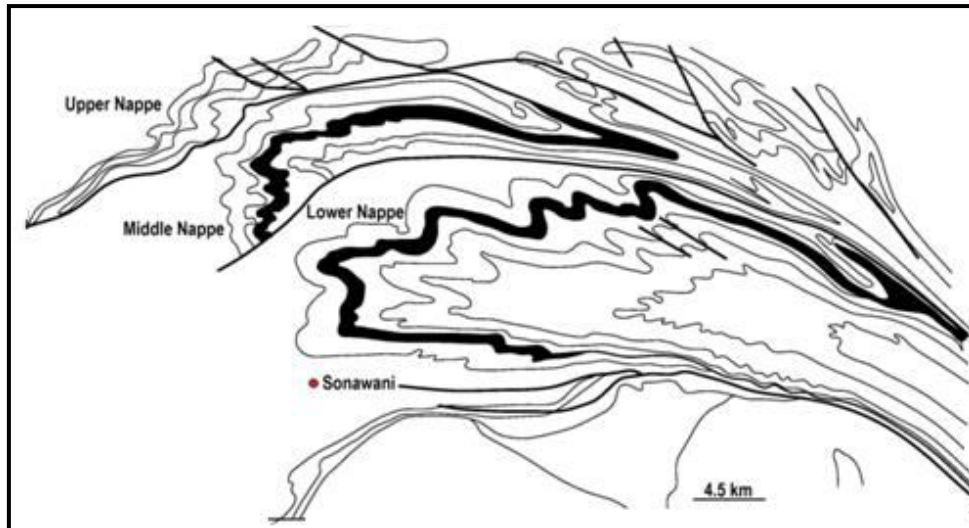
Figure 1A : The Sonawani Fold Neppes are large scale recumbent folds with amptitudes more than 10 kms have been recognized in the Sonawani since more than 100 years., but the mechanical process by which they form is until now not fully understood. The dynamics of fold neppe formation with similar numerical models that are used to study buckle-folding. The basic process of neppe formation in order to allow a physically based tectonic reconstruction of the neppes. Representative cross section of the Sonawani Nappe which is a large scale recumbent fold with a prominent overturned limb (left). Finite element simulation of a basic scenario of fold Nappe under far-field simple shear (right).

the eastern end of the belt the rocks are of epi-grade, with phyllites containing sericite chlorite, offrelite etc. Garnet, sturolite, biotite and kyanite come in furtherwest, while in the northwest and north, sillimanite pyroxene and iron-garnets are well developed. The middle stripe in which the Sonawani gneiss is prominently developed (Fig: 1 B, C and D) represents probably the root zone of the former mountain belt which has since been largely planed off. The Sonawani suffered final folding and metamorphism between 1330 and 1340 million year (Sarkar, et al, 1964)

1.1. Conceptual models for tectonic Nappes

    The Sonawani are a mountain range made of tectonic Nappes, and have long been a testing ground for revolutionary ideas in tectonics, such as the Nappe theory (e.g R.C..Buton, L.L.Fermer, Dr.W.D. West, Pro. A.C Benerji, Pro. M.N. Saha, Mr. D.S. Bhttacharji, Mr.B.C. Gupta, Dr. Heron Mr. Sondhi, and M.S. Krishnan). There is a general agreement that the overall tectonic structure of the Sonawani represents an imbricate Nappe stack, and that the emplacement of the Nappes happened in an ordered succession such that the stacked order from top to bottom reflects the palaeogeographic position from internal to external, respectively .However, the discovery of high pressure and ultra-high pressure ((U)HP metamorphism, which invoked mantle depth tectonism that opened an extensive debate on the dynamics of tectonic Nappes. Related to the Nappe forming mechanism, the present tectonic models of convergent orogens can be described by a combination of two end-members: 1) thrust and 2) intrusion models (Fig.2). 1) Thrust models generally approximate the orogen as wedge-shaped continua with a rigid buttress behind and a subducting lithospheric slab beneath (e.g. Brandon, 2004; Konstantinovskaia and Malavieille, 2005; Platt, 1986). In the thrust model the dominant process of Nappe formation is accretion of tectonic units from the subducting plate into the above orogenic wedge by thrusting (brittle and/or ductile). This thrusting generates a dominant top-to-the-foreland shear sense in the Nappes. In the thrust model the rocks building the orogen exist within crustal depth (say < ~60 km; e.g. Platt, 1986). Exhumed rocks did not subduct significantly into the mantle, and uplift and exhumation of HP rocks occurs by under-plating accompanied by isostatic uplift, extension in higher levels of the wedge and erosion (e.g. Platt, 1986). Thrust models can successfully explain the coherent and imbricate Nappe stacking and the first-order
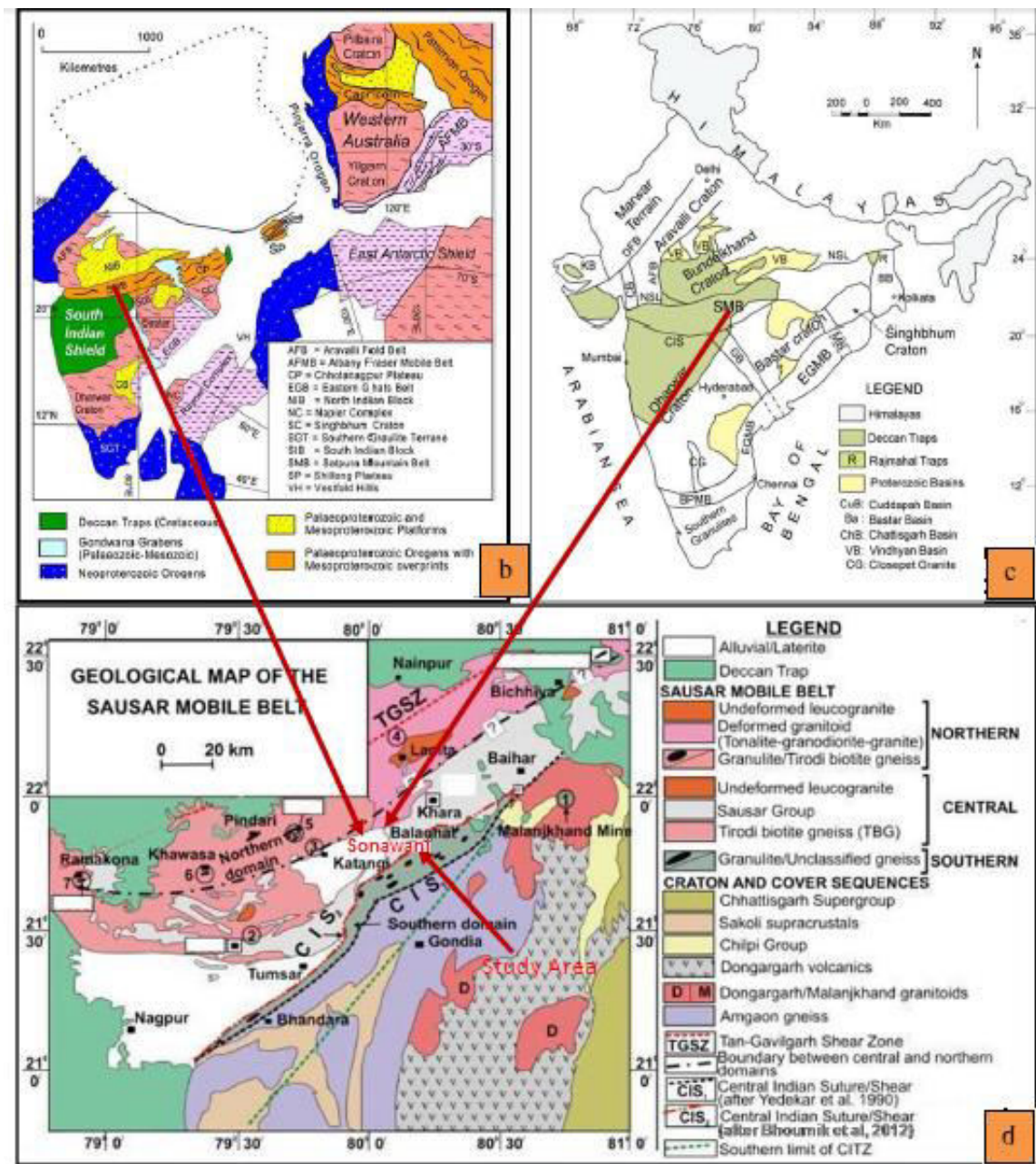
Figure. 1 B: Map showing of tectonic units of India (after Mohanty, 2011, (C) after Pradhan et al., 2010.) D: Geological map of Central India showing the study area (after Bhowmik et al., 2012).

structural observations in the Sonawani However, in the magnitudes of pressure estimated from observed minerals in exhumed rock in the Sonawani has increased steadily. It is generally assumed that the pressure estimates from observed (U)HP rocks is close to the lithostatic pressure so that metamorphic pressure is a good indication of maximum burial (Jolivet et al., 2003). It is expected that metamorphic pressure is a fine indicator for maximum burial poses a fundamental problem to the thrust model, namely to account for the large burial depth of (U) HP rocks (Stefan, M. et al 2014). Maximal pressure estimates in the Sonawani indicate depths in excess of 100 km. Nappe formation at these mantle depths cannot be explained anymore by the thrust model because the UHP units intrude into the orogenic wedge from mantle depth. 2) In intrusion models (U)HP rocks are subducted to mantle depths and return to crustal depths usually by buoyancy driven or tectonically forced flow (see Hacker and Gerya, 2013; Warren, 2013, for recent reviews on the formation and exhumation of (U)HP rocks). In intrusion models the Nappes are formed during the return flow of the UHP rocks, depicting thrust shear sense at the bottom and normal-fault shear sense at the top of the Nappe.
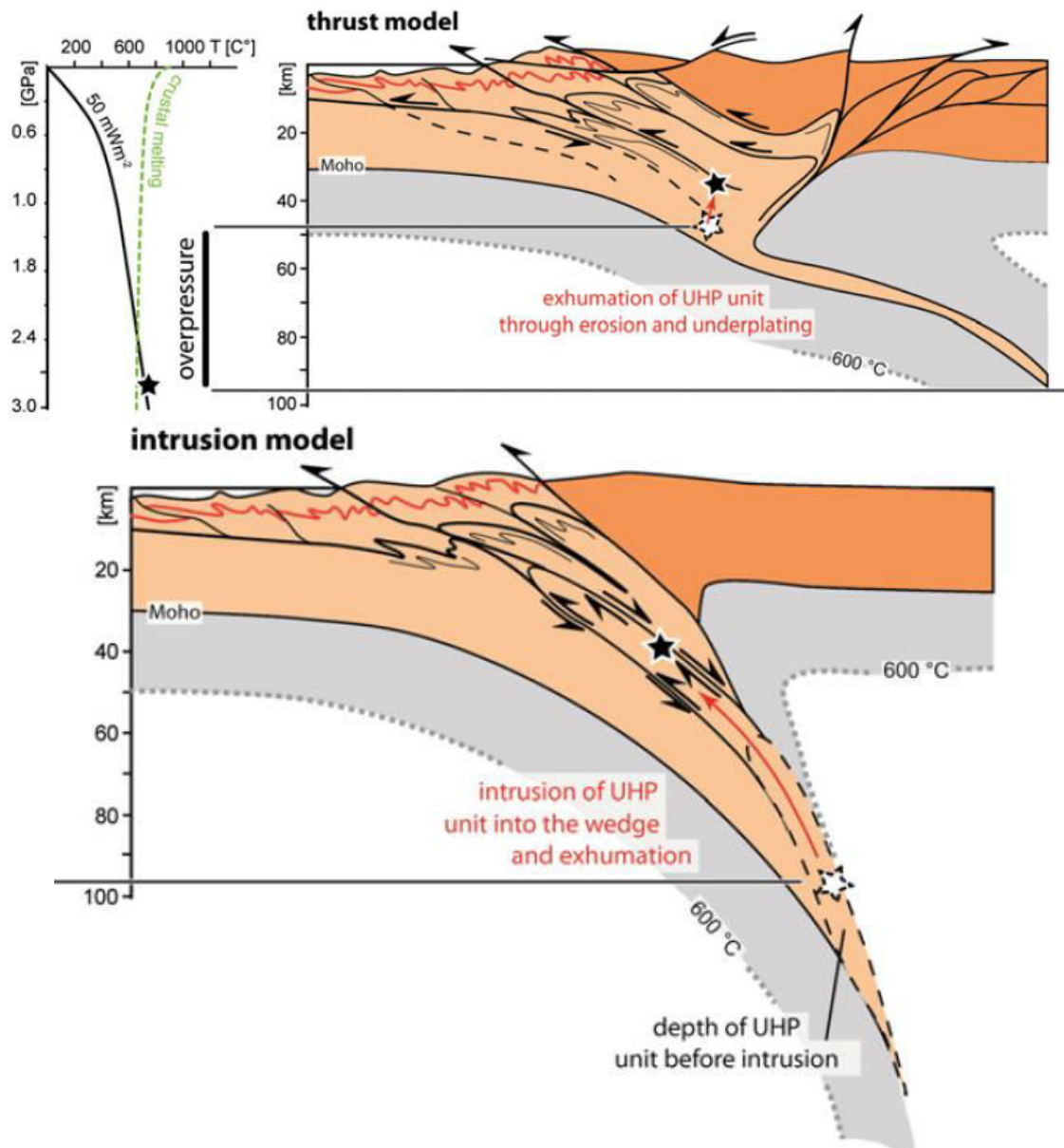
4

Figure. 2. Sketch of the thrust model and the intrusion model for the formation of a tectonic Nappe that exhibits UHP rocks and is situated in an imbricate Nappe stack. In the thrust model the Nappe exhibits a penetrative top-to-the-foreland shear sense, whereas in the intrusion model the Nappe exhibits a major extensional shear zone at the top with a top-to-the-hinterland shear sense. In both models the shearing must be active during the pressure peaks.

In the field, the latter normal-fault shear sense is diagnostic for the intrusion model since it does not form in the thrust model (e.g. Butler et al., 2013; Fig.2). In the intrusion model the rocks are extruded from mantle depths by channel flow (e.g. England and Holland, 1979) and then intrude as Nappes into the structurally higher imbricate crustal Nappe stack (e.g. Butler et al., 2013; Escher and Beaumont, 1997). Numerical intrusion models could reproduce the first-order patterns of data-calibrated pressure-temperature (P-T) time paths of the Sonawani. However, there are several problems with intrusion models, such as: First, a fundamental kinematic (rheology and driving force independent) feature of the intrusion scenario is the upward movement of tectonic units from depths > 100 km that requires the presence of a major extensional shear zone in the hanging wall of each exhuming (U)HP unit (e.g. Butler et al., 2013). However, in several well-studied Nappes of the Sonawani exhibiting (U) HP rocks such a major extensional syn-(U)HP shear zone has yet to be identified. By contrast, the earliest and dominant coherent structures recorded along the upper boundary of these (U) HP units are top-to-the-foreland shear zones that are consistent with the thrust model, and were active under

amphibolite- or green schist facies conditions. Particularly, for the Sonawani (U) HP conclude that 1) all rock units of the Sonawani massif were sheared and juxtaposed together within a top-to-the-foreland ductile contractional shear zone, 2) the (U) HP unit was incorporated into the orogenic pile before extension, and 3) the extensional structures in the Sonawani do not define the upper boundaries of tectonic wedges formed during extrusion. Second, numerical intrusion models are often unable to generate a coherent and imbricate Nappe stack. For Sonawani it could reproduce the first-order features of P-T paths, but the authors also state that the corresponding structural evolution of the orogenic belt in their models is dominated by large-scale curl. Such large-scale curl generates a repetition of tectonic units (Nappes) with rocks from the same paleo-geographic domain along a section across the orogeny. However, the kinematics of a large-scale curl and the related repetition of tectonic units are in contrast to the observed imbricate Nappe stack of the Sonawani. Third, intrusion models often require extremely fast exhumation rates of several centimetres per year as suggested by the estimation from P-T-time data of (U) HP rocks assuming lithostatic pressure; for example ~3.4 cm/yr for the Sonawani show that the exhumation rate required for the Sonawani considerably exceeds the estimated rates of convergence of ~5 mm/yr during the time of exhumation. Such high exhumation rates should lead to high erosion rates and elevated upper crustal shortening. In contrast, the reconstruction of structure shows that upper crustal horizontal shortening in the Foreland Basin is only ~25 km between 35 and 30 Ma what contrasts the ~ 124 km of horizontal movement estimated from the P-T-time path of the Sonawani during the same period (assuming a pressure-to-depth relation and a subduction channel dip of ~40°). Suggested tectonic overpressure is one possible solution to this Nappe problem".

1.2. Tectonic pressure

The prime argument against the application of a thrust model to the Sonawani is the assumption that pressure recorded by (U) HP rocks indicates maximum burial depth, and the same assumption is a major argument for an intrusion model. If significant tectonic overpressure (i.e. the pressure deviation from the lithostatic pressure, e.g. Mancktelow, 2008) existed during the evolution of the Sonawani, and if the correspondingly higher-than-lithostatic pressures would have been recorded by exhumed (U)HP rocks, then (U)HP rocks would have formed in significantly less depth, and thrust models including tectonic overpressure could be applicable to the Sonawani (Fig.2). Therefore, the quantification of tectonic overpressure during tectonic Nappe formation is essential to eventually determine whether a thrust model or an intrusion model can better explain the tectonic evolution of the Sonawani.

There is debate on tectonic overpressure as a reason for (U) HP metamorphism in crustal rocks. This debate on overpressure is closely related to the strength of rocks or to the magnitudes of differential stress in the Earth's lithosphere (e.g. Kanamori, 1980). From a physical point of view dynamic pressure (i.e. over- and under-pressure) must exist in deforming rocks and, therefore, the main debate concerns the magnitude of the overpressure. It is used here that the term "significant overpressure" in the context of (U)HP tectonism if overpressure is more than 20% of the pressure recorded in an exhumed rock (e.g. > 400 MPa for a rock indicating 2 GPa), and hence if overpressure affects in a crucial way the pressure to depth conversion of (U)HP rocks. Several studies suggest that the magnitude of the pressure deviation from the lithostatic pressure is insignificant because crustal rocks are weak and the differential stress that controls natural deformation is low (e.g. Brace et al., 1970; Burov et al., 2001; Jolivet et al., 2003 and references therein). Brace et al. (1970) reported GPa-level strength magnitudes ranging from 0.2 to ~1.1 GPa for metamorphic rocks; yet, they rejected their experimental result on the assumption that under geological conditions 1) the presence of fluids, 2) the low strain rates, and 3) the high temperatures would reduce the strength of rocks to low magnitudes. However, recent experimental studies indicate that even the weakest HP crustal lithology (omphacite-bearing rocks) can support stresses of ~ 1 GPa under geological conditions for temperatures ~500 °C and strain rates between 10^{-13} and 10^{-15} s^{-1}; a result derived from micromechanical-based extrapolation to geological conditions (e.g. Moghadam et al., 2010). Furthermore, a rheology-independent force balance analysis based on the gravitational potential energy around the Tibetan plateau indicates that the deviation of the horizontal stress from the

lithostatic pressure in the lithosphere must be at least 70-200 MPa in average across the lithosphere in order to statically support the Tibetan plateau (e.g. Molnar and Lyon-Caen, 1988; Molnar et al., 1993; Schmalholz et al., 2014). Finally, rock deformation experiments with quartz show the formation of coesite for pressure significantly smaller than 2.5 GPa (e.g. Hirth and Tullis, 1994). Hirth and Tullis (1994) suggest that the transition from quartz to coesite is not controlled by the pressure (mean stress) but by the largest principal stress. The experimental result of Hirth and Tullis (1994) questions the applicability of a simple pressure to depth relation.

1.3. Numerical simulations for convergent orogens

The numerical simulations of convergent orogens conclude that tectonic overpressure in crustal rocks is insignificant (e.g. Butler et al., 2013; Li et al., 2010) while some studies conclude that tectonic overpressure can be significant (e.g. Mancktelow, 2008; Schmalholz and Podladchikov, 2013). The main reasons why many numerical studies focusing on the formation and/or exhumation of (U)HP rocks do not report significant tectonic overpressure in exhumed crustal rocks are the following: 1) In many simulations either very low internal friction angles in the entire crust (both upper and lower crust) are applied from the start of the simulation (e.g. 7° was used by Li et al., 2010, for their reference model), or strain softening that reduces the friction coefficient after a small amount of strain to values usually around 4° is applied (e.g. Butler et al., 2013, reduce the friction coefficient for all crustal rocks from initially maximal 15° to 4°). However, data from deep drilling and induced seismicity experiments show that friction angles in the upper crust must not be so small, and can also be ~30° in the presence of hydrostatic pore pressure (e.g. Lockner et al., 2011; Townend and Zoback, 2000). A consequence of the applied low friction angles in the entire model crust is that most crustal rocks in these models deform at low frictional strength implying a brittle/frictional deformation. Moreover, the effective viscosities of lower crustal rocks can vary orders of magnitudes depending on the considered flow law (e.g. Rybacki and Dresden, 2004). Hence, models with either a weak or strong lower crust are both mechanically feasible. However, if models assume the weakness of all crustal rocks a priori, then it is of course difficult to develop significant tectonic overpressure in crustal rocks in such models. Consequently, such "weak crustal" models have little predictive power concerning the fundamental question whether significant tectonic overpressure may or may not develop in crustal rocks. 2) In many numerical models reporting insignificant tectonic overpressure either a subduction zone itself or a prominent large-scale weak zone are utilised to pre-define the location of subduction and hence the subduction channel. Such models have little predictive power concerning the question whether or not a subduction channel may develop in a self-consistent way because its presence is prescribed ab initio (e.g. Butler et al., 2013; Li et al., 2010; Yamato et al., 2008). 3) Many numerical models reporting insignificant tectonic overpressure apply a homogeneous upper and lower crust. However, both weak and strong inclusions embedded in rock can cause significant stress and pressure variations (e.g. Schmid and Podladchikov, 2003), and such pressure variations in a heterogenous crust can potentially generate locally significant tectonic overpressure (Moulas et al., 2014). 4)

A more technical, but still important, point is that several numerical models reporting insignificant tectonic overpressure use plastic strain softening whereby the friction coefficient reduces with strain to a certain low value (e.g., Butler et al., 2013). Such type of strain softening causes a mesh-dependency of the numerical results, in particular the thickness of shear zones (e.g. Deborst and Sluys, 1991). Therefore, strictly speaking, the numerical solution is non-convergent because the results do not tend to a stable orientation and thickness with increasing numerical resolution. Numerical results including strain softening become grid-convergent if certain mathematical regularizations are applied (e.g. gradient plasticity, Cosserat model; e.g. Bazant and Jirasek, 2002), which provide resolution independent numerical results. However, such regularisation requires the a priori specification of the shear zone thickness.

It is presented here that numerical models of lithospheric shortening with a configuration that differs in the four points mentioned above from numerical models reporting insignificant tectonic overpressure. In this model it is applied that a friction angle of 30° in the crust, and use a strong

rheology for the lower crust. It is not introduce that a subduction zone or a prominent weak zone. Also, it is not considered a homogeneous but a heterogeneous crust in which one weak and three strong inclusions of kilometre scale are present. Finally, it is not applied that plastic strain softening but consider thermo-mechanical coupling and thermal weakening due to viscous heating and temperature dependent viscosities. Recently, Thielmann and Kaus (2012) presented a systematic numerical study, and showed that such viscous heating is able to generate lithospheric-scale strain localisation, shear zones and subduction zones in a self-consistent way. Here, it is numerically resolved that the pressure and temperature anomalies inside such shear zones, and also within and around crustal heterogeneities. In order to prove the robustness and accuracy of the results, it is shown that the applied algorithm conserves energy and fulfils the bulk force balance during large-strain lithospheric deformation.

The presented simulations are performed to quantify potential values of tectonic overpressure and temperature during the formation of a crustal shear zone that eventually becomes a tectonic Nappe. In a tectonic context the simulations mimic thrusting and Nappe formation during continental collision (Fig.2). However, the model configuration is considerably simplified, that is, an already established subduction zone or orogenic wedge is not considered, and assume that the colliding continents behave as a single rheological unit after closure of the intervening ocean basin (cf. Burg et al., 2002). There are two main reasons for this simplified model configuration: 1) It is required to keep the model simple so that the results are comprehensible, and can also be easily reproduced by other researchers. 2) The characteristics of the Sonawani Nappe are highly debated. Many studies assume that there was a lithospheric break-up during extension, and that the basins consisted mainly of newly formed crust and lithosphere. Other studies assume that there was no lithospheric break-up or only minor newly formed lithosphere, and that consisted of hyper-extended margins and exhumed sub-continental mantle. Many numerical simulations include a significant length of lithosphere (300-600 km) that generates a significant slab pull (e.g. Sizova et al., 2012; Butler et al., 2013). It is not considered that a newly formed lithosphere in order to test a different tectonic situation for which a compressive force, and not slab pull, is the driving force of the orogeny. The model configuration is also applicable to a geodynamic scenario often referred to as intra-continental subduction that has been suggested for some HP Nappes of the Sonawani . Synthetic P-T paths are presented for selected tracer points during Nappe formation. The synthetic P-T paths generated in the simulations can hence be considered as the dynamic contribution during Nappe formation, and this contribution can be "added" to the "background" P-T path that resulted from the preceding (with respect to Nappe formation) burial by subduction and Nappe stacking, and the later exhumation by mainly extension and erosion. Numerically modelling the entire evolution of the Sonawani is beyond the scope of this study. Nevertheless, it is discussed that the implications of the results and their potential applicability to (U) HP tectonism in the Sonawani.

2. Mathematical model

2.1. Governing equations

The mathematical model is based on continuum mechanics and is formulated for two dimensional (2-D) plane strain deformation (e.g. Mase, 1970). The force balance equation is

$$\frac{\partial \sigma_{ij}}{\partial x_j} - \rho a_i = 0 \tag{1}$$

where i and j run from 1 (horizontal) to 2 (vertical; repeated indexes are summed), σ_{ij} are the components of the total stress tensor, x represents the spatial coordinates, ρ is the density, the column vector $a_i = [0 \ g]^T$ with superscript^T representing the transpose of a vector), and g is the gravitational acceleration. The density is a linear function of temperature

$$\rho = \rho_0(1 - aT) \tag{2}$$

where ρ_0 is the density at 0 °C, a is the thermal expansion coefficient and T the temperature. Density variations are only considered for body forces when multiplied by g (Boussinesq approximation). The total stress is

$$\sigma_{ij} = -P\delta_{ij} + T_{ij} \tag{3}$$

where P is pressure (negative mean stress; $P = -\sigma_{ij}/2$), σ_{ij} is the Kronecker delta and T_{ij} are the components of the deviatoric stress tensor. The rheology is described with an incompressible linear Maxwell model for viscoelasticity

$$\dot{\varepsilon}_{ij} = \dot{\varepsilon}_{ij}^v + \dot{\varepsilon}_{ij}^e += \frac{1}{2\eta}T_{ij} + \frac{1}{2G}\frac{DT_{ij}}{Dt} \tag{4}$$

where $\dot{\varepsilon}_{ij}$ are the components of the deviatoric strain rate tensor, superscripts v and e indicate viscous and elastic deviatoric strain rate tensors, respectively, η is the effective viscosity, G is the shear modulus, t is the time and D/Dt represents the upper convected time derivative of the stress tensor components (e.g. Schmalholz et al., 2001). The components of $\dot{\varepsilon}_{ij}$ for incompressible materials are

$$\dot{\varepsilon}_{ij} = \frac{1}{2}\left(\frac{\partial v_i}{\partial x_j} + \frac{\partial v_j}{\partial x_i}\right) \tag{5}$$

where v is the velocity. The applied viscous flow law represents dislocation creep, and the corresponding effective viscosity (see appendix A) is given by

$$\eta = f\mu\left(\frac{E_{II}^v}{\dot{\varepsilon}_B}\right)^{\frac{1}{n}-1}\exp\left[\frac{Q}{nR}\left(\frac{1}{T} - \frac{1}{T_c}\right)\right] \tag{6}$$

where μ is the reference viscosity if $T = T_c$ and $E_{II}^v = \dot{\varepsilon}_B$, and E_{II}^v represents the square root of the second invariant of the viscous (dissipative) part of the strain rate tensor

$$E_{II}^v = \frac{T_{II}}{2\eta}, \tag{7}$$

where T_{II} is the square root of the second invariant of the deviatoric stress tensor

$$T_{II} = \sqrt{\tau_{11}^2 + \tau_{12}^2}. \tag{8}$$

The parameter E_{II}^v is used to describe the strain rate dependence of the viscosity η because η is sensitive only to the dissipative part of the deformation and not to the elastic part that is conservative (i.e. the elastic deformation is reversible). The quantity $\dot{\varepsilon}_B$ is a reference strain rate that is here the bulk shortening strain rate used in the numerical simulation, f is a multiplier to increase or decrease the effective viscosity relative to an effective viscosity resulting from rock deformation experiments (Table 1), Q is the activation energy, T_c is a characteristic temperature that is here the initial temperature at the Moho in the model, n is the power law stress exponent, and R is the gas constant. The value of μ can be calculated from published flow laws based on laboratory experiments (see appendix A and Table 1).

The stresses are limited by a yield stress, τ_y, described by a Mohr-Coulomb criterion:

$$\tau_y = b\cos(\theta) + P\sin(\theta) \tag{9}$$

where b is the cohesion and (θ) the angle of internal friction. If stresses are equal to or exceed the yield stress, τ_y, i.e. $T_{II} \geq \tau_y$, then the effective viscosity is reduced iteratively (Picard iterations) until the force balance is satisfied (e.g. Lemiale et al., 2008; Schmalholz and Maeder, 2012). Therefore, the effective viscosity is

$$\eta = \eta \qquad \text{if } \tau_{II} - \tau_{Y,} < 0$$
$$\eta = \tau_Y/2E_{II} \qquad \text{if } \tau_{II} - \tau_{Y,} \geq 0 \tag{10}$$

where E_{II} is the square root of the second invariant of the strain rate tensor

$$E_{II} = \sqrt{\left(\frac{\partial v_x}{\partial x}\right)^2 + \frac{1}{4}\left(\frac{\partial v_x}{\partial y} + \frac{\partial v_y}{\partial x}\right)^2} \tag{11}$$

This viscoplastic formulation is suitable to limit the stresses according to the Mohr-Coulomb criterion but not to model the exact evolution and spacing of frictional-plastic shear bands (Poliakov et al., 1994), which is also not the aim of this study.

The applied equation to calculate heat transfer is

$$\rho c \frac{\partial T}{\partial t} = \frac{\partial}{\partial x_i}\left(k \frac{\partial T}{\partial x_i}\right) + H_R + H_D \tag{12}$$

Table.1
Material properties

	A $(Pa^{-n}s^{-1})$	n	Q (kJ/mol)	G (GPa)	b (MPa)	θ	α (K^{-1})	H_R (W/m^3)	k (W/m/K)	ρ (kg/m^3)	c (J/kg/K)	f
Upper crust	5.07×10^{-18}	2.3	154	10	10	30	3.2×10^{-5}	0.5×10^{-6}	2.5	2700	1050	1
Lower crust incl.-model	3.20×10^{-20}	3.0	276	10	10	30	3.2×10^{-5}	0	2.5	2850	1050	1
Lower crust	5.05×10^{-28}	4.7	485	10	10	30	3.2×10^{-5}	0.2×10^{-6}	2.2	2850	1050	0.57
Mantle	2.50×10^{-17}	3.5	532	10	Pe*	Pe*	3.2×10^{-5}	0	3.0	3300	1050	1
Weak inclusion	5.05×10^{-28}	4.7	485	10	10	30	3.2×10^{-5}	0.2×10^{-6}	2.2	2850	1050	0.1
Strong incl. upper crust	5.07×10^{-18}	2.3	154	10	10	30	3.2×10^{-5}	0.2×10^{-6}	2.2	2850	1050	50
Strong incl. lower crust	2.50×10^{-17}	3.5	532	10	10	30	3.2×10^{-5}	0	3.0	3300	1050	1

Creep parameters A, n and Q . Upper crust corresponds to granite, lower crust to diabase and mantle to olivine. See text for explanation of symbols. Pe*: The stresses in the mantle are limited by a Peieris creep law. For the lower crust in the inclusion model (Fig.3A) another flow law was used (Maryland Diabase from Carter and Tsenn, 1987) than for the lower crust in the lithospheric model (Fig.3B).

Where c is the specific heat, k the thermal conductivity, H_R the radiogenic heat production and H_D the heat generated by viscous-plastic dissipation with

$$H_D = \frac{\tau_{11}^2}{2\eta} + \frac{\tau_{22}^2}{2\eta} + \frac{\tau_{12}^2}{\eta} \tag{13}$$

No advection terms are considered for heat transfer because a Lagrangian formulation is used where the temperature is advected with a deforming mesh.

For surface processes simulations, a simple model is applied to simulate the basic features of erosion and sedimentation. A constant erosion rate of 1 mm/yr is applied when the surface is above a reference level that is here the surface at the left model side. If the surface is below the reference level it is moved back to the reference level assuming that the topographic depression is filled instantaneously with sediments. This simple model is intended to mimic the first order large-scale features of surface processes, namely the redistribution of surface loads, and does not aim at providing a realistic landscape evolution.

2.2. Numerical methods

The system of non-linear partial differential equations resulting from the above equations is discretised and transformed to a linear system of equations with the finite element method (FEM; e.g. Bathe, 1996). The Above equations are solved using a mixed formulation with Crouzeix-Raviart triangles with quadratic velocity shape functions enhanced by a cubic bubble function and discontinuous linear interpolation for the pressure field (so-called P2 +— P1 element; e.g. Thomasset, 1981). Incompressible fluids are considered and apply the penalty method in combination with Uzawa iterations to enforce a divergence free velocity. The non-linearity due to the power-law rheology and

the yield stress is treated with Picard iterations. A Lagrangian approach with re-meshing is used to handle the large strains. The model geometry is described through external and internal contours with up to 2000 nodes on a single contour. The numerical mesh is generated with the algorithm Triangle (Shewchuk, 2002). Both the finite element mesh and the interfaces are moved with the resulting velocity fields using an explicit Euler forward scheme. The time step is adaptive depending on both the maximal velocity in the model and the maximal grid deformation between two consecutive time steps. Time steps vary between 200 and 2000 yrs, and usually three Picard iterations are performed for each time step. Once the quality of the finite element mesh becomes unsatisfactory it is regenerated with Triangle using the evolved model geometry defined by the contours. Interpolation of variables from the new to the old mesh is done using the MATLAB function "Tri Scattered Interp". A free surface stabilisation algorithm developed by Kaus et al. (2010) is also implemented in the finite element algorithm. Typical simulations require 600 to 1000 time steps. A horizontal velocity is applied at the left and right boundary to cause shortening. The basics of the applied finite element algorithm are described in Schmalholz et al. (2008), and the algorithm relies on the fast finite element method solver MILAMIN (Dabrowski et al., 2008).

Additionally, a similar set of equations has been solved numerically with the finite difference method (FD) to test and benchmark the finite element algorithm. The finite difference algorithm is based on an Eulerian-Lagrangian method, and the general features of the algorithm are described in Gerya (2010). The incompressible Stokes and heat equations are discretised on an Arbitrary Lagrangian-Eulerian (ALE) grid. A classical staggered grid (e.g. Gerya, 2010) is employed for solving the Stokes equations and a cell-centred scheme coupled to a second order backward dif-ferentiation formula (BDF) method is used to discretise the transient heat equation. This discretisation offers a first order spatial accuracy (L1 norm) in the presence of material boundaries (Duretz et al., 2011). Solutions to the coupled velocity-pressure Stokes and heat equations are obtained by using the parallel direct solver PARDISO (Schenk and Gartner, 2004, 2006). The advection equation is solved on a set of Lagrangian markers that carry the material properties, the temperature and the stresses of the deforming media. The position of the markers is updated at each time step using a second order in space explicit Runge-Kutta solver. Mapping between the markers and the grid solutions is achieved by a 1-Cell distance-weighted interpolation (Yamato et al., 2012). A Picard iteration scheme is employed coupled to a line search algorithm in order to solve for the non-linearity inherent to the power law flow law.

3. Pure shear inclusion model for shear zone formation

3.1. Model configuration

The model geometry is a rectangular box, 75 km wide and 30 km high (Fig.3A). A circular inclusion with a radius of 3 km is in the model centre. The boundary conditions for the velocities are: free-slip on all sides and horizontal and vertical velocities are applied at the boundaries to cause pure shear horizontal shortening and vertical extension. The velocities are modified every time step to maintain a constant background rate of deformation, $\dot{\varepsilon}_B$ (i.e. the ratio of the difference of the horizontal boundary velocities to the current model width), of $5\times10^{-14}s^{-1}$. The heat flow through all boundaries is zero. The initial temperature is constant and is 400 °C. Only a viscous flow law is applied (no elasticity, no plastic stress limitation). The material parameters for the homogeneous matrix are the ones for a typical lower crustal rock and for the circular inclusion the ones for a typical upper crustal rock (Table 1). In these simulations gravity and radioactive heat production are not considered.

3.2. Results

A series of numerical simulations are conducted based on two different numerical methods and with different numerical resolution to show the robustness of the numerical solution. These simulations model the formation of shear zones around a weak circular inclusion. Fig.4 shows the distribution of E_{II} in the vicinity of the weak inclusion after, 20% of bulk shortening. FEM results were obtained using an unstructured mesh with resolutions ranging from ~40,000 degrees of freedom
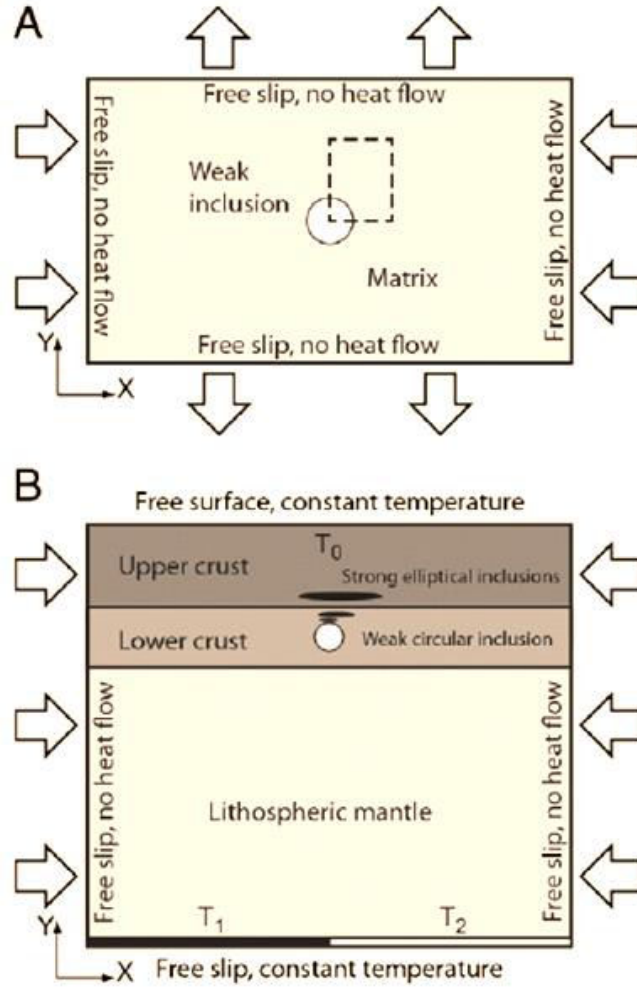
Figure. 3. Model configurations. A) Pure shear model with inclusion. The model is 8 km wide and 500 m high containing a circular inclusion with 3 km radius. Both matrix and inclusion exhibit a power-law flow law, the matrix with parameters for the lower crust and the inclusions with parameters for the upper crust (Table 1). The initial temperature is 400 °C everywhere. The constant pure shear bulk shortening rate h = 5× 10⁻¹⁴s⁻¹.The dashed rectangular area indicates the location of the zoom window utilized in Figs. 28and 4. B) Lithospheric shortening model (Schmalhoiz. et al 2014)

(40 kd of) to ~1Mdof (Fig. 4 A to C). FD results were calculated on regular meshes containing up to 2.4Mdof (Fig. 4 D to F). Results of both numerical methods agree and show that the thickness of the shear band is independent of the numerical resolution. Also, magnitudes of EII inside the shear band are indendent on the numerical resolution. It is also tested the finite strain evolution of the shear zones. Fig. 5 shows the distribution of EII for three stages of background shortening (0.5%, 20% and 30%). Results are shown for both FEM and FD results obtained with the highest resolution used in Fig. 4. Passive rotation of the shear bands occurs during pure shear horizontal shortening leading to a progressive steepening of the shear zone angles from 45 to 60°.

Because there is no analytical solution for the large strain evolution of the shear bands it is further tested the algorithms with respect to energy conservation. If the numerical algorithms conserve energy, then all the mechanical work (W) done in the viscous fluid is dissipated and must be converted into thermal energy (E). Both W and E have been calculated for each numerical time step, and then numerically integrated over the total simulation time. E is given by
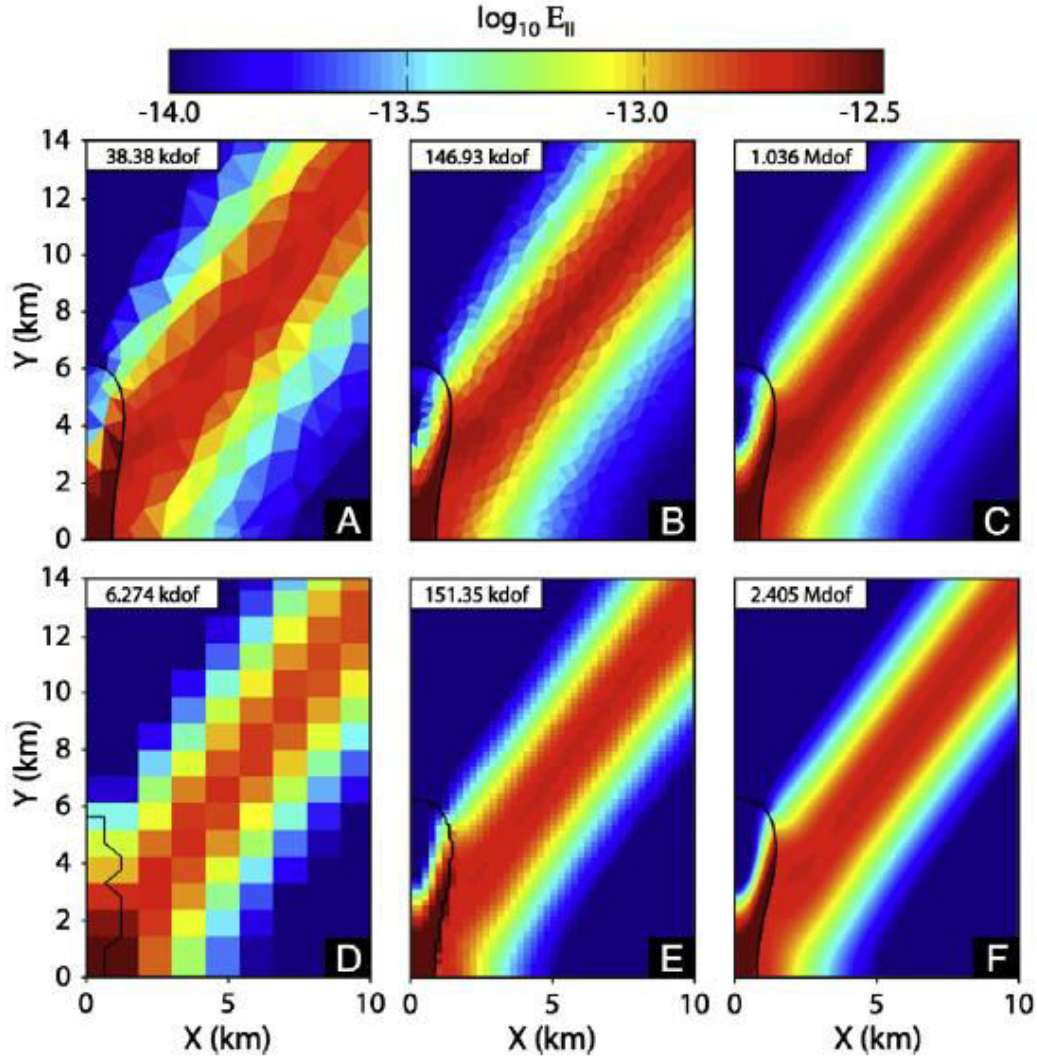
$$E = \iint (\rho c T)\, dV dt. \qquad (14)$$

12

Figure. 4. Colour plots of the square root of the second strain rate invariant *(E_{II})* **after 20% of bulk shortening (model time is 0.14 Ma) of the model shown in Fig.3A. Panels A to C show results of the finite element algorithm for three different resolutions (kd of is degrees of freedom times thousand), and panels D to F show results of the finite difference algorithm. Both methods yield mesh-insensitive results with increasing numerical resolution. The shear band thickness and values of E_{II} remain constant with increasing resolution.**

The volume (area in 2-D) integral was evaluated numerically over the model area for each time step and the time integral has been evaluated with an explicit Euler scheme. W is given by

$$W = \int \left[\oiint (\sigma_{ij} v_i n_j) ds \right] dt. \tag{15}$$

At each of the four model boundaries only the normal stresses and the normal velocities have been used to numerically integrate the product of stress and velocity along each boundary. For the FEM simulations with a triangular mesh the results have been interpolated on a rectangular grid to perform the numerical integrations over the model area and model boundary. Both E and W are plotted versus bulk shortening for both the high resolution FEM and FD simulations in Fig.6.After 30% shortening the maximum difference between E and W was ~0.5%. The results therefore show thermo-mechanically consistent and conservative behaviour.

For both methods (FEM and FD) the numerical results converge to a common conservative solution in which the modelled shear zones are characterised by a finite width. Pressure, stress, strain rate and temperature can therefore be accurately calculated throughout the initiation and deformation
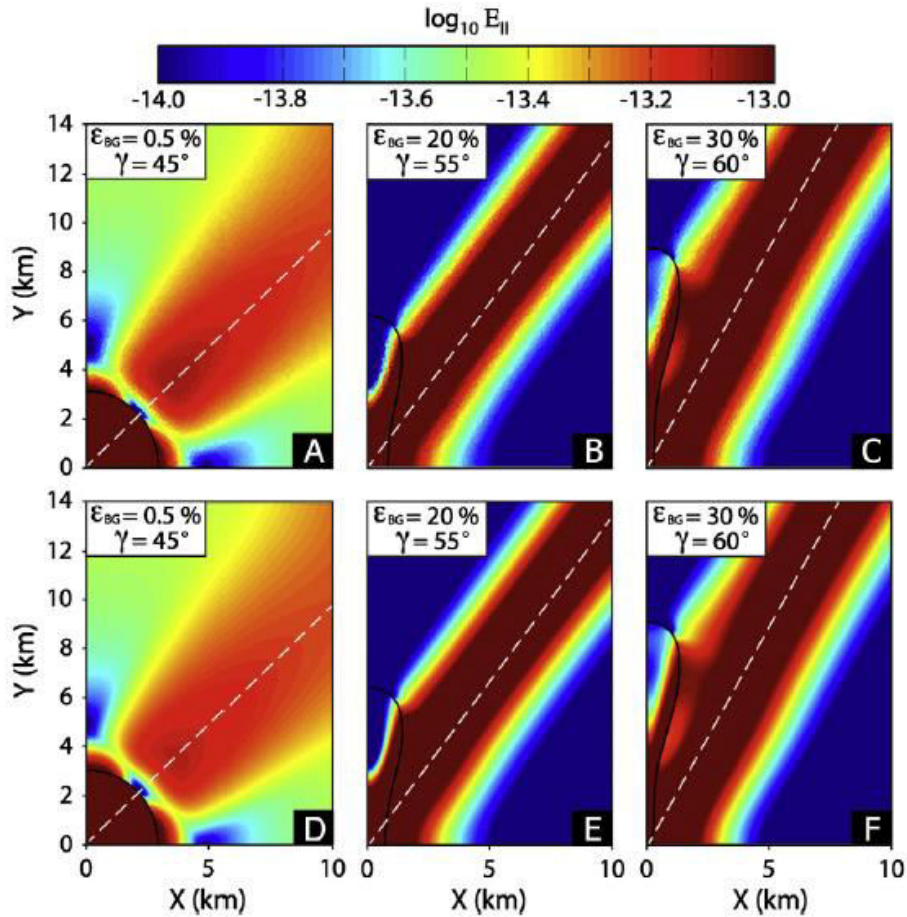
Figure. 5. Colour plots of the square root of the second strain rate invariant (E_{II}) for three stages of bulk shortening (ε_{BG}) of the model shown in Fig.3A Panels A to C show results of the finite element algorithm for the highest resolutions shown in Fig.4C, and panels D to F show results of the finite difference algorithm for the highest resolutions shown in Fig.4 F. In both simulations the shear bands initiate with an angle (γ) of 45° and are then progressively rotated during horizontal pure shear shortening up to an angle of 60°.

of the shear zones. The thermal weakening due to viscous heating and temperature-dependant viscosity allows for memorising the weakening and the resulting shear zones can be maintained, advected (e. g. rotated), and deformed with progressive deformation. Since both methods (FD or FEM) exhibit mesh-independent behaviour, the results can be potentially reproduced by any current numerical modelling tool. The simulations have been also performed with the FEM algorithm using a viscoplastic rheology and the results also confirm the energy conservativeness of the algorithm for viscoplastic rheology.

4. Lithosphere model with weak and strong inclusions

4.1. Model configuration

The basic model configuration is shown in Fig.3B. The model is initially 594 km wide and 150 km high. The upper crust has an initial thickness of 40 km and the lower crust of 14 km. The weak circular inclusion has an initial radius of 3 km and is in a depth of 47 km in the horizontal middle of the model. The strong elliptical inclusion in the upper crust has an initial maximal width of 20 km and thickness of 1.5 km. The strong inclusion is in a depth of 37 km and 3 km to the right of the middle of the model. One strong elliptical inclusion in the lower crust has an initial maximal width of 4 km, a thickness of 0.5 km, is in a depth of 43.5 km and in the horizontal middle of the model.
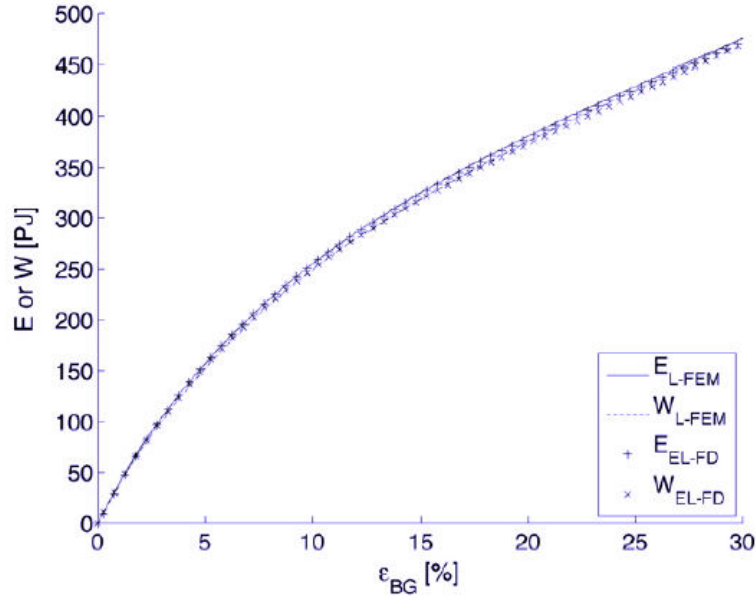
Figure. 6. Evolution of total thermal energy (E) and mechanical work (W) with progressive shortening for the model shown in 3A. The energies have been calculated with the finite element (FEM) and finite difference (FD) method. For both simulations E and W are nearly identical indicating that the numerical algorithm conserves energy during thermo-mechanical coupling. The results based on the FEM and the FD agree representing a successful benchmark of the algorithms.

A second strong elliptical inclusion in the lower crust has an initial maximal width of 8 km, a thickness of 1 km, is in a depth of 42.5 km and 2 km to the right of the middle of the model. The contours defining the inclusions consist of 721 nodes and the inclusions are numerically well resolved. The boundary conditions for the velocities are: the lateral and the bottom boundaries are free slip boundaries and the top boundary is a stress free surface. Horizontal velocities are applied at the lateral boundaries to cause horizontal shortening with a constant bulk rate of shortening; $\dot{\varepsilon}_B$, of $8 \times 10^{-5}S^{-1}$.the boundary velocity is decreasing during the shortening to maintain a constant bulk rate.

4.2 Results

Fig.7 shows the model evolution with the formation of a crustal-scale shear zone for three stages of lithospheric shortening. Black lines indicate the limits between different model units and grey lines indicate a passive mesh to visualise the deformation. This passive mesh does not correspond to the numerical mesh. The passive mesh indicates also the erosion in the right side of the model and sedimentation in the left side. At 5.5% shortening a shear deformation in the weak, lower part of the upper crust is visible which is mainly gravity driven because the warmer right model side slightly uplifts relative to the left side. At 12% shortening a shear zone that dips to the right develops around the weak inclusion. At 23% shortening one major crustal-scale shear zone dipping to the right has formed. The black passive lines and the grey grid show that the shear zone generated a geometry resembling a fold Nappe.

Fig.8 shows zooms of the distribution of τ_{II} and of the tectonic overpressure, $P_O = P - P_L$, for three shortening stages. P_L is the lithostatic (or hydrostatic) pressure, that is, the pressure resulting only from the weight of the overlying rocks. At 3.7% shortening high $\tau_{II}$and high P_O is at the top of the lower crust and inside the strong inclusions in the lower crust. Between the inclusions in the lower crust the values of P_O are generally higher than the values of τ_{II}. Laterally away from the weak inclusion $P_O \approx \tau_{II}$ as predicted by analytical results for a friction angle of 30° (e.g. Petrini and Podladchikov, 2000). Only the upper half of the weak inclusion is surrounded by strong material (Fig.8A), but the entire weak inclusion exhibits a few hundred MPa of P_O while values of τ_{II} are significantly smaller. Shortening a shear zone that dips to the right develops around the weak inclusion.
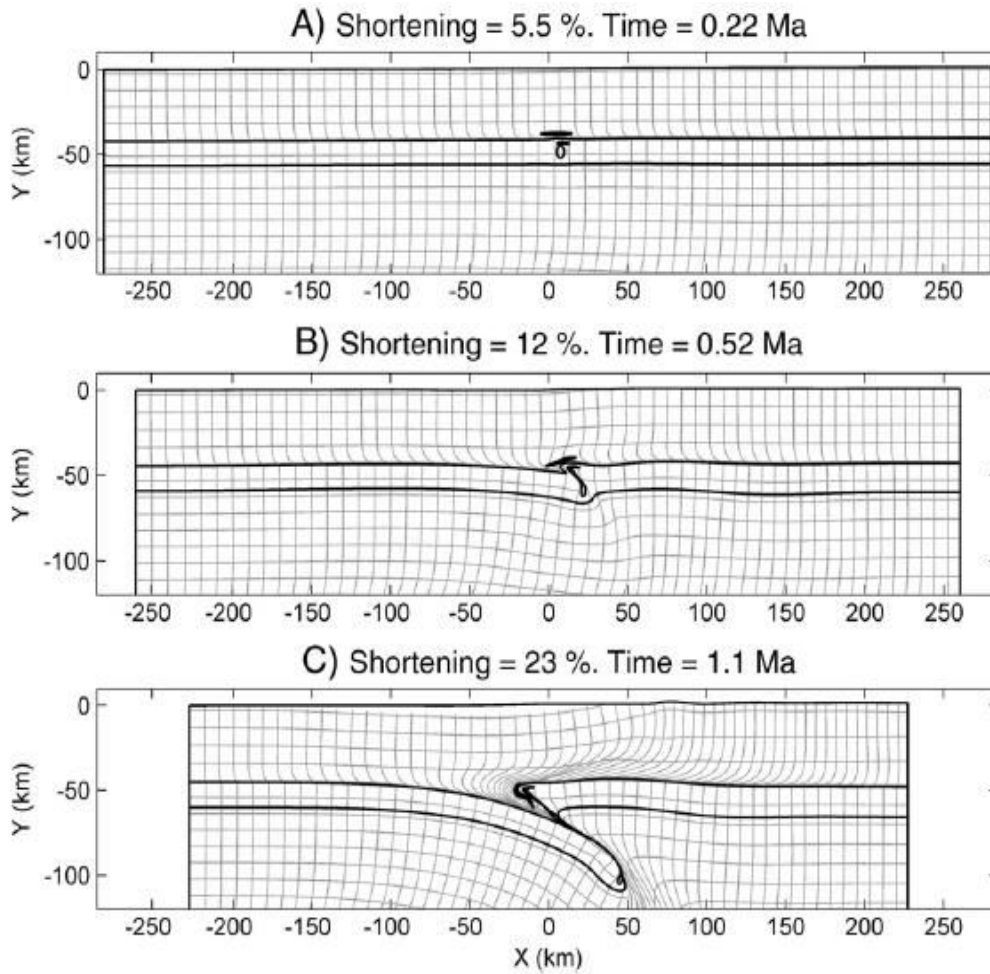
15

Figure. 7. Geometry of the lithospheric model for three stages of horizontal shortening (in %). Black lines indicate boundaries between numerical model units, and the grey lines indicate a passive mesh (not the numerical mesh) visualising the finite strain.

At 23% shortening one major crustal-scale shear zone dipping to the right has formed. The black passive lines and the grey grid show that the shear zone generated a geometry resembling a fold Nappe. At 7.5% shortening P_O in the weak inclusion is ~500 MPa while τ_{II} in and around the weak inclusion is significantly smaller. The results indicate that a continuous strong material around the weak inclusion (i.e. a "pressure vessel") is not necessary to generate significant P_O ~500 MPa within a weak inclusion. P_O in the crust has reduced and an area of high P_O is visible at the top of the mantle lithosphere where the crust-mantle boundary develops a shear zone. At 12% shortening PO has further decreased within the lower crust but is still high within the strong inclusions in the lower crust. There is also high P_O in the lower part of the weak inclusion and to the left of the weak inclusion (Fig.8 F), whereas values of τ_{II} in the same regions are lower (Fig.8E).

Fig.9 shows horizontal profiles of vertically depth-integrated quantities and of quantities that are maximal in the vertical profiles. Such profiles are important to test whether the numerical results fulfill the bulk force balance of the entire lithosphere, and to quantify how the integrated strength of the lithosphere varies with time and space. The continuum mechanics force balance equations require that in a litho-sphere under compression, with a stress free surface and zero shear stresses at the base, the vertical integral of σ_{xx} $(\overline{\sigma_{xx}})$must be constant along the horizontal direction (e.g. Molnar and Lyon-Caen, 1988; Schmalholz and Podladchikov, 2013; Schmalholz et al., 2014). On the other hand, the vertical integral of P $(\bar{P})$, P_O $(\overline{P_O})$ and τ_{xx} $(\overline{\tau_{xx}})$can vary in the horizontal direction. Fig.9A shows
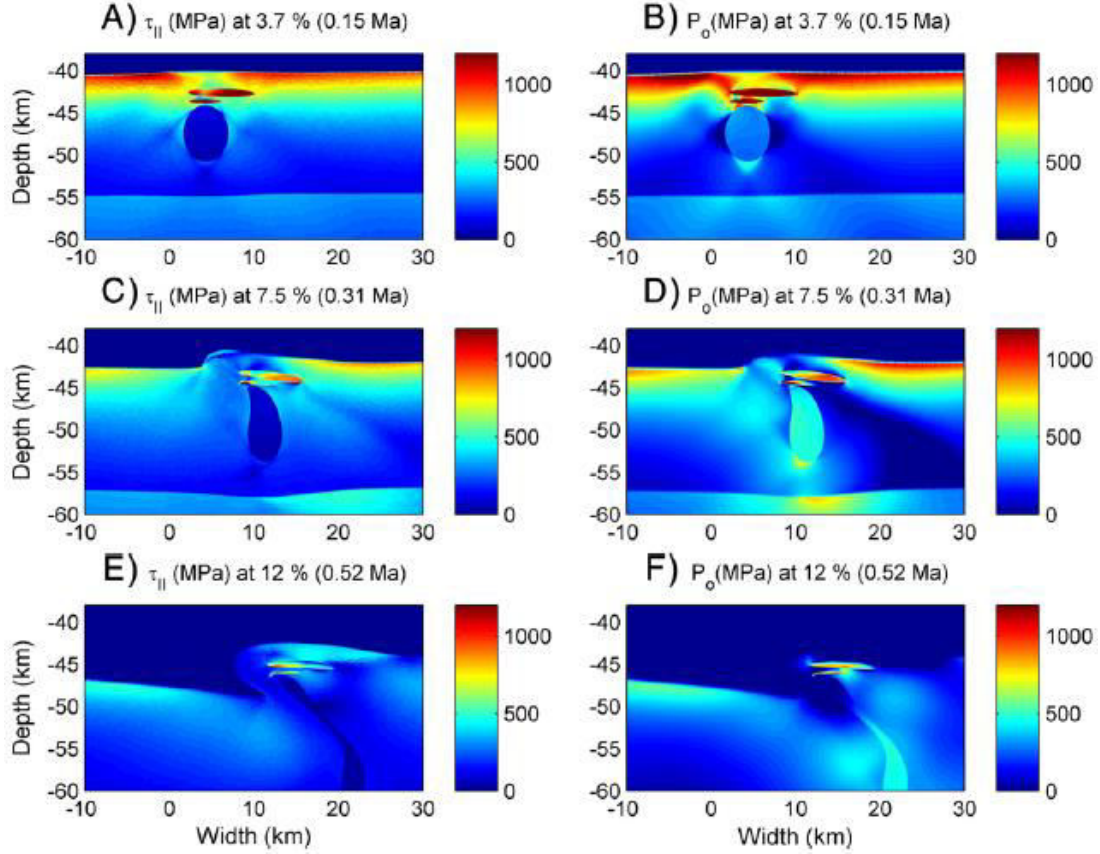
Figure. 8. Zooms into colour plots of the square root of the second stress invariant (τ_{II} and of the tectonic overpressure (PO) for the lithosphere model (Fig.3B) at three stages of bulk shortening (in %).

values of $\overline{\sigma_{xx}}$ calculated from the numerical results for the three shortening stages of Fig. 8. $\overline{\sigma_{xx}}$ is constant in space indicating that the numerical results fulfill the bulk force balance throughout the large strain deformation. $\overline{P}$, $(\overline{P_O})$ and $\overline{\tau_{xx}}$ vary in the horizontal direction (Fig. 9B, C and D). The maximal values of P_O and τ_{II} within a vertical column of the lithosphere vary significantly horizontally and temporally (Fig.9E and F). The maximal P_O in the crust is ~2.2 GPa at 3.7% shortening whereas the maximal τ_{II} is ~ 1.5 GPa showing that the magnitude of P_O can be significantly larger than the magnitude of T .The largest P_O occurs in the strong inclusion and $P_O > \tau_{II}$ is caused by the effect of a strong elliptical inclusion (e.g. Schmid and Podladchikov, 2003;see also Moulas et al. 2014).

Fig.10 shows the evolution of selected P-T paths (calculated for tracer points that have been followed throughout the simulation), and the distribution of P for the three shortening stages of Fig.8. The three light-grey dashed lines indicate isotherms for 500 (upper line), 600 and 700 °C (lower line, Fig.10C). Although tracer points were never deeper than 50 km some tracer points reach the UHP facies field (P > 2.6 GPa). These tracer points exhibiting UHP were located inside the strong inclusions in the lower crust where the largest P_O in the crust occurred throughout the simulation. Other tracer points that are close to the shear zone reach temperatures > 700 °C. The pressure at the beginning of the P-T paths corresponds to the lithostatic pressure before the onset of shortening. The highest pressure in one selected P-T path is ~3.4 GPa which corresponds to a value that is nearly a factor of 3 larger than the initial lithostatic pressure (~1.2 GPa). Since the rock did not undergo significant burial, the increase in pressure is nearly inclusively due to tectonic stresses. The pressure and temperatures of tracer points that are in the upper crust and are at 12% shortening below and above (i.e. in the foot and hanging wall, respectively) the Nappe of lower crustal rocks vary significantly less than the pressure and temperature inside the Nappe. Therefore, the pressure and

temperature recorded in the Nappe of lower crustal rock are considerably larger than the pressure and temperature of the upper crustal rocks below and above the Nappe.

Fig.11 shows the evolution of P and T with time for the tracer points shown in Fig.10. Pressure peaks are reached after a few hundred thousand years after the onset of the deformation. Temperature peaks are always reached a few hundred thousand years after the pressure peaks. The maximal $P \sim 3.4$ GPa decreases to ~ 1.7 GPa with ~ 700 kyrs. Assuming a lithostatic pressure and a density of 2800 kg/m^3, these pressure values would indicate a vertical exhumation of ~ 62 km within 700 kyrs providing an apparent exhumation rate of ~ 9 cm/yr. This exhumation rate has the same order of magnitude than the exhumation rate of ~ 3.4 cm/yr that has been estimated for the Sonawani, and the 9 cm/yr are within the error range of the 3.4 cm/yr estimate. The maximal temperature increase due to viscous heating is ~ 200 °C.

5. Discussion

5.1.Results concerning inclusions and shear bands

The presented inclusion models (Fig.3A) were performed with different numerical algorithms at different resolutions. The shear zones developing due to viscous heating and related thermal weakening exhibit resolution-independent thickness and magnitudes of E_{II} (Fig.4). The numerical algorithms are also conservative with respect to the resulting thermal and mechanical total energies (Fig.6). Furthermore, horizontal profiles of depth-integrated horizontal total stresses (Fig.9A) indicate that during the lithospheric simulations the bulk horizontal force balance is fulfilled throughout the entire large strain deformation exhibiting significant variations in deviatoric stresses and pressures. These results show that the numerical results are robust and that the resulting stress and pressure magnitudes in and around the shear zones are numerically accurate.

Weak inclusions that are only partly surrounded by stronger rocks can exhibit significant P_O even if the values of τ_{xx} and T_{II} in these inclusions are significantly smaller (Fig.8). The P_O inside the weak inclusion is even significant if only the upper half of the inclusion is surrounded by stronger
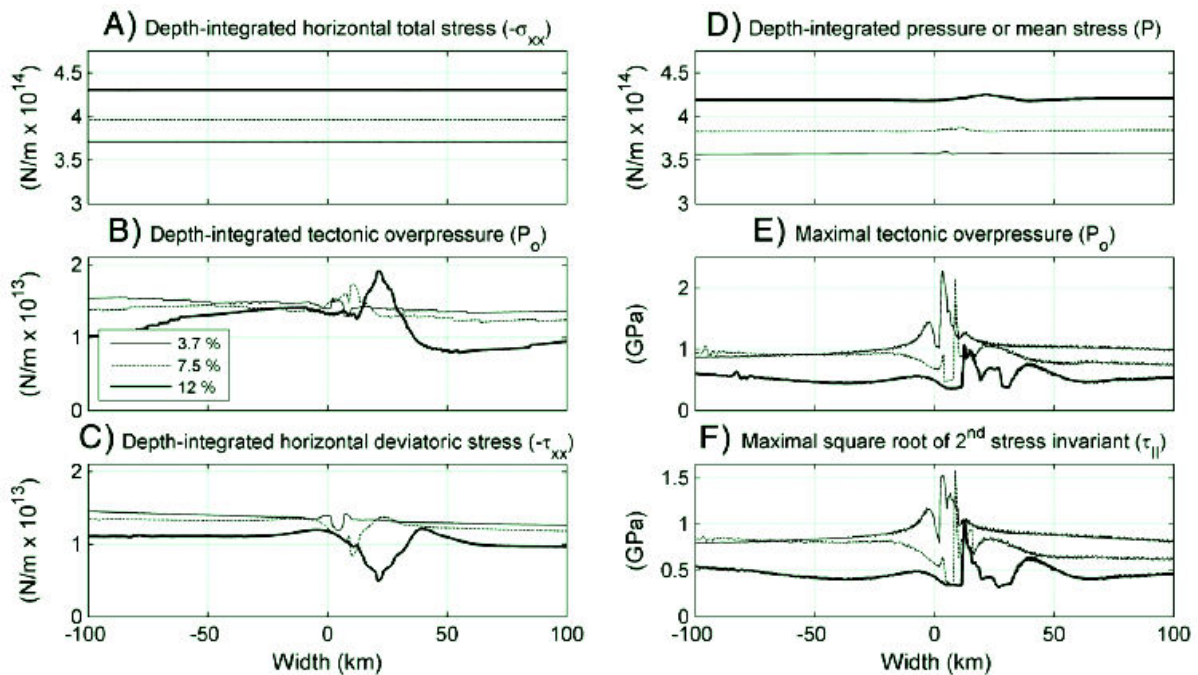

Figure. 9. Horizontal profiles of depth-integrated quantities and maximal quantities within vertical profiles for the three stages of bulk shortening (in %) shown in Fig.8. The legend in B) applies to all panels.

18

rocks and the lower part of the inclusion is surrounded by weak rocks (Fig.8), because the overpressure in the weak inclusion is necessary to maintain a constant depth-integrated horizontal total stress when the deviatoric stresses are decreased due to thermal weakening. It is therefore not necessary to have a continuous strong "vessel" around a weak inclusion to generate significant overpressure in the weak material.

5.2.Model configuration and parameters

For the lithospheric simulation, the flow law for dry Maryland diabase (Afonso and Ranalli, 2004) for the lower crust, but decrease the effective viscosity slightly (Table 1). For the mantle and the two strong inclusions in the lower crust, the flow law for dry peridotite is used (Afonso and Ranalli, 2004). The Peierls creep mechanism is only activated in the mantle, and stresses in the strong inclusions are limited by the Mohr-Coulomb criterion. The two inclusions should not represent only mantle rocks but rather any kind of strong rock inside the lower crust. For example, the flow law for dry anorthite provides similar high stresses than the flow law for the dry olivine (e.g. Rybacki et al., 2006). For the lithosphere model, a friction angle of 30° is used. Data from deep drilling and seismicity induced experiments show that friction angles of crustal rocks in the presence of a hydrostatic fluid pressure can be ~30° (e.g. Townend and Zoback, 2000), and agree with friction angles corresponding to Byerlee's law (Byerlee, 1978) for hydrostatic fluid pressure. However, many models simulating the formation and exhumation of (U)HP rocks in subduction channels use low friction angles < ~15° for the entire crust (e.g. Butler et al., 2013; Li et al., 2010). Zhu et al. (2013) used even 0° for several model units (e.g. sedimentary rocks, upper oceanic crust or serpentinised mantle) in a 3-D numerical model.

An initial temperature of ~640 °C is used at the crust-mantle boundary in a depth of 54 km which is a temperature that is similar to Moho temperatures estimated for mobile belts (e.g. McKenzie et al., 2005). It is applied that a thick crust of 54 km, because it is assume that Nappe formation took place in a depth between 40 and 50 km (e.g. Platt, 1986). In the model high deviatoric stresses ~ 1 GPa occur only within a thin (few kilometres) layer at the top of the lower crust, and within strong inclusions (Fig.8). This thin but strong layer is sufficient to generate significant overpressure and shear heating during lithospheric shortening. Such horizontal shortening of layered rheological units, as applied in the model, is also a typical model configuration for analogue models of continental collision (e.g. Burg et al., 2002; Sokoutis et al., 2005). Numerical models using low friction angles and weak flow laws in the entire crust exclude the possibility of such a thin, strong layer a priori, and hence exclude the possibility of generating significant overpressure in crustal rocks. The lower crustal layer in the model should not representonly typical lower crustal rocks (e.g. granulite), but any kind of strong crustal rock at lower crustal pressure and temperature conditions in depth > 40 km ($P > $ ~1 GPa and $T > $ ~500 °C).

5.3. Application to the Sonawani

5.3.1. Nappe structure and kinematics

The Sonawani exhibit three prominent (U)HP regions, namely the Upper, the Middle, and the Lower . Maximal pressure and temperature estimates are ~3.5 GPa and ~750 °C for the Upper ~2.6 GPa and ~590 °C for the Middle , ~2.5 GPa and ~560 °C for the Lower Nappe (Fermer,1916). Assuming the correctness of these estimates and an average density of crustal rocks of 2800 kg/m^3 a pressure of 2.5 GPa corresponds to a burial depth of ~91 km and 3 GPa to ~109 km. According to the current paradigm for the formation and exhumation of (U)HP rocks all three (U)HP regions were formed by subduction into the mantle and by their subsequent exhumation from great depth (e.g.Butler et al, 2013;Hacker and Gerva 2013; Li et al, 2010; Warren, 2013). All three (U)HP regions are the Sonawani Nappes, and they are generally interpreted to exhume from depth in a subduction channel. The Nappes below and above the (U)HP Nappes usually exhibit considerably lower pressure suggesting that the Nappes were emplaced according to the intrusion model (e.g. Butler et al; 2013). The results suggest an alternative mechanism for the generation of (U)HP conditions that does not
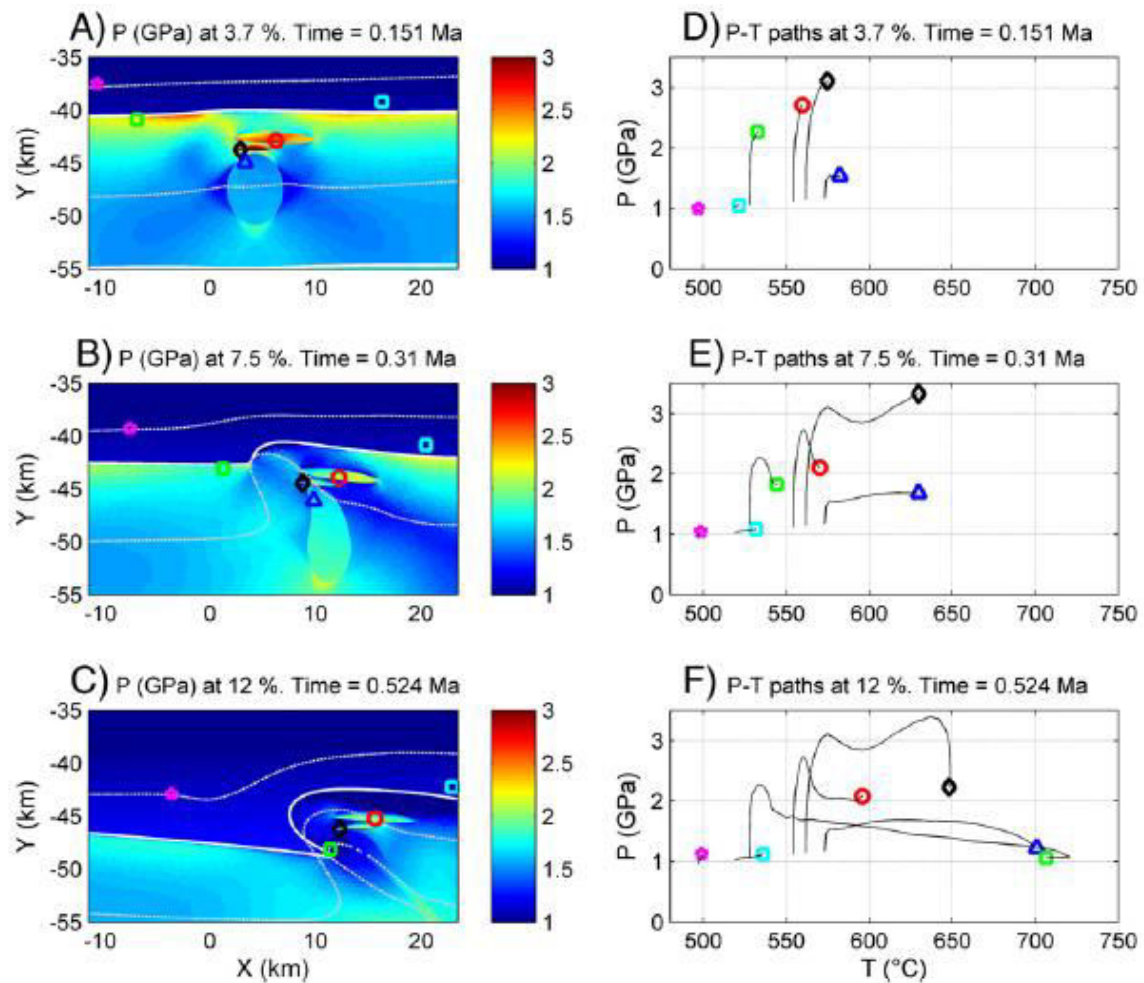
Figure. 10. Pressure-temperature (P-T) paths for selected tracer points (symbols in D to F) and zooms into colour plots of the pressure (P) indicating the position of the tracer points (A to C) at the three stages of bulk shortening (in %) shown in Fig.8. In A to C the grey dashed lines indicate isotherms for 500 (uppermost line), 600 and 700 °

require deep subduction of crustal rocks. The numerical simulations demonstrate that it is physically feasible to generate tectonic overpressures ~2 GPa and hence pressures of ~3 GPa at crustal depths between 40 and 50 km   according to the thrust model. The requirement for such tectonic overpressure is a thin crustal level with a strength corresponding approximately to the strength predicted by Byerlee's law (friction angle ~30°), and the existence of weak and strong inclusions within such layer.

The modelled Nappe exhibiting (U) HP is sandwiched between rocks exhibiting significantly lower pressure and temperature (Fig.10C and F); a situation that is typical for (U) HP Nappes in the Sonawani. Moreover, in the models the units below and above the (U)HP Nappe, and the (U)HP Nappe itself exhibit the same top-to-the-foreland shear sense; a finding again typical for observations in Nappes in the Sonawani (e.g. Avigad et al, 2003; Pleuger and Podladchikov, 2014)

Further geological observations from the Internal, the Nappe show geometrical and kinematic similarities in the models (Fig.12). The Internal is an imbricated and folded sequence of older Sonawani series, the younger Chilpi-Ghat series and Archaen sediments which includes also basement slices. The structural position of the Internal Belt below and in front of the Nappe (Fig.12) suggests a more external (northward) paleogeographic position with respect to the Sonawani Nappe.
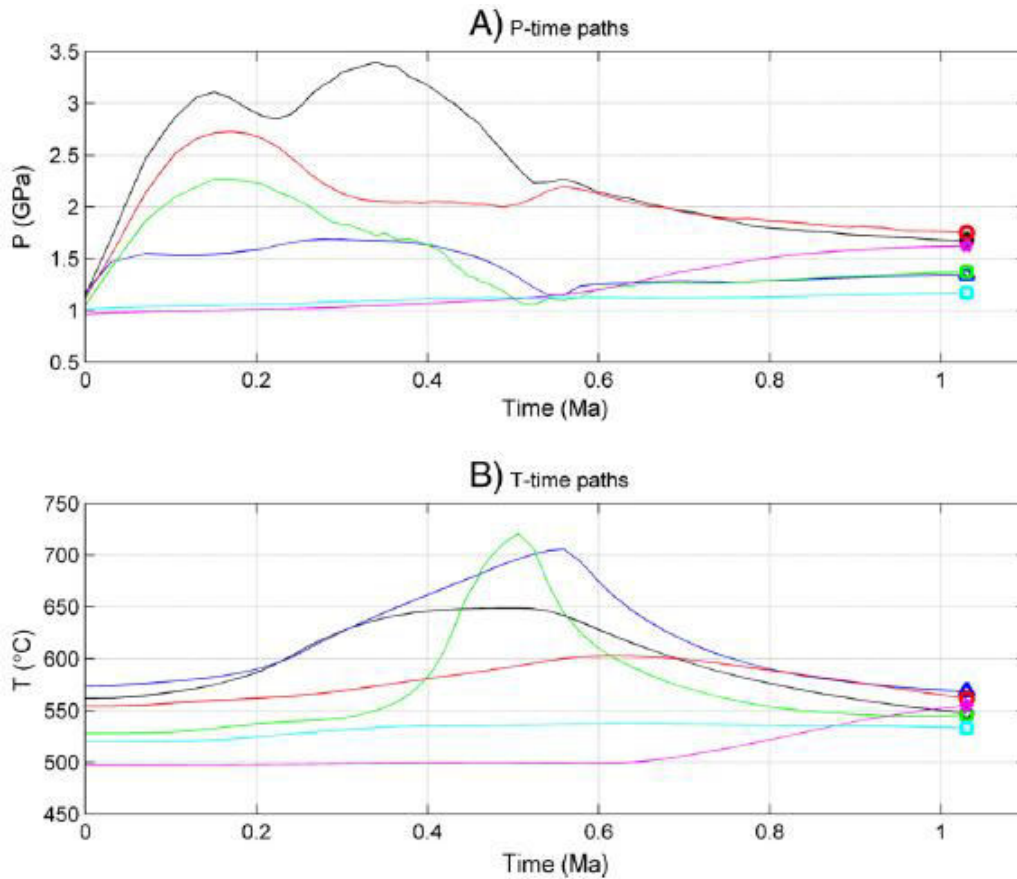
Figure. 11. Evolution of pressure (A) and temperature (B) with time for the tracer points shown in Fig.10.
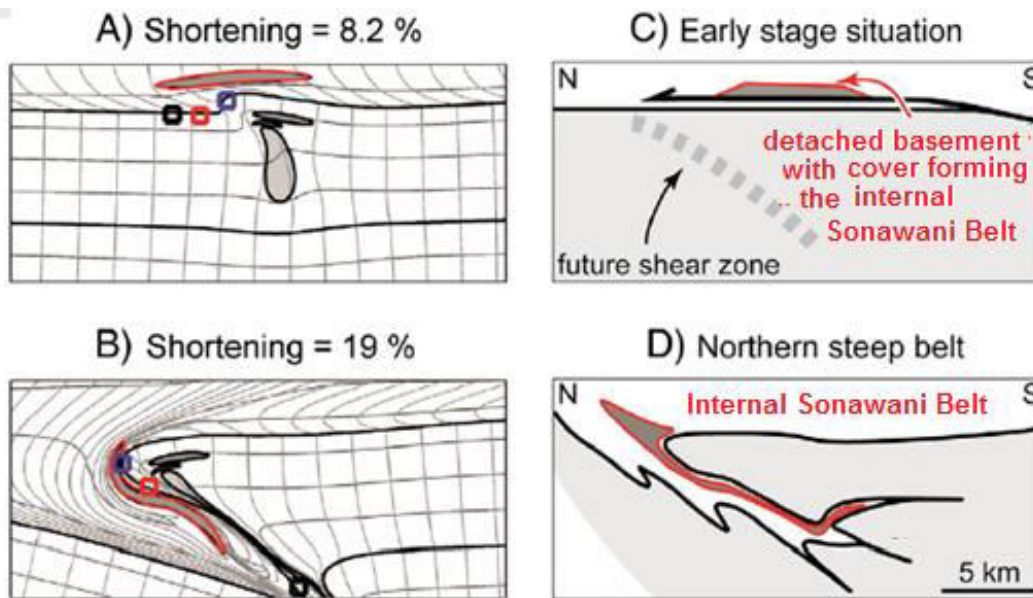

Figure. 12. A) and B) show numerical results for the kinematic evolution of the fold Nappe, the deformation of the inclusions and the motion of three marker points at two different stages of shortening(in%). Black lines are boundaries between model units and grey lines indicate passive mesh (not the numerical mesh,cf. Fig.7). C) and D) shows a sketch of an interpretation for the evolution of the Sonawani Nappe and the Internal Sonawani Belt (see text for explanation).The Internal Chilpi Ghat Belt may have been detached from the underlying manganese basement and may have been dragged below the Sonawani Nappe during the fold Nappe formation; similar to the ellipse (with red boundary)in A)and B)
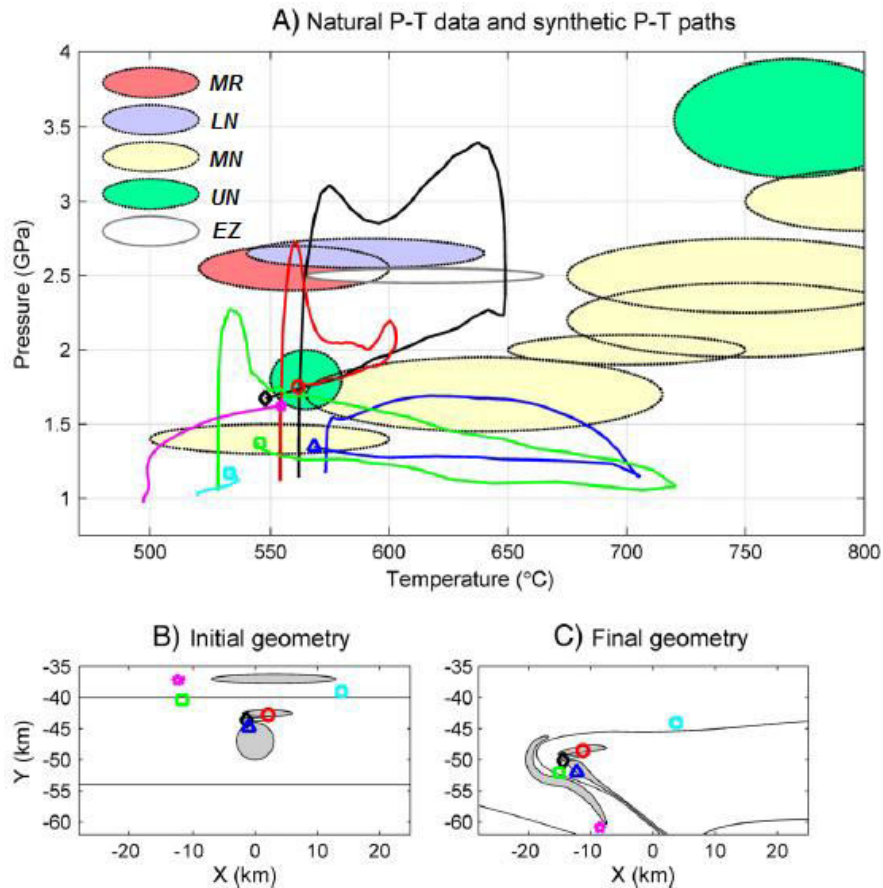
Figure. 13. Pressure-temperature diagram with maximal estimates from the Upper Nappe (UN), Middle Nappe (MN), Lower Nappe (LN), Manganese Rocks (MR)and the Eclogite Zone (EZ) together with numerically calculated P-T paths for tracer points shown in the two subplots below (the same tracer points as in Figs. 10 and 11). The lower pressure domain for the Upper Nappe is from the hanging wall of the UHP unit...

In contrast, recent stratigraphic correlations with classical and well established Sonawani stratigraphy suggests that the sediments had a more internal (southward) paleogeographic position with respect to the lower Nappe . In the latter scenario, the Nappe and the associated slices have been detached from its basement-substratum and thrust with a top-to-the foreland transport direction above the early stage of the Sonawani orogeny. Subsequently, with increasing shearing and fold Nappe development the Internal Belt has been wrapped around and dragged below the front. In this Nappe model, the ellipse inside the upper crust could represent the Internal Sonawani Belt that was initially located above the developing fold Nappe. During the Nappe formation this ellipse is dragged below the Nappe (Fig.12). Therefore, the model of fold Nappe formation can explain how tectonic units that are initially structurally above a Nappe are placed structurally below this Nappe during the Nappe formation supporting the stratigraphic observation of Glaster et al. (2010, 2012).

The Nappe developing in the model is a fold Nappe with an overturned lower limb. Such fold Nappe geometry is also observed in other basement Nappes in the Sonawani. In the fold Nappe model the hinge point at the front of the Nappe is more or less stable whereas the hinge point at the lower bottom of the fold Nappe migrates indicating that rock units from the foot wall can be incorporated into the Nappe during its formation (Fig.12).

From a structural and kinematic point of view the orogenic wedge model of Platt (1986) explains well the formation of the Sonawani imbricate Nappe stack by thrusting. A similar thrust model for the Sonawani (Fig.2) in which the tectonic Nappes are mainly fold Nappes that are formed dominantly by ductile thrust-sense shearing, and in which tectonic overpressure and shear heating

22

have contributed to the observed pressure and temperature peaks in crustal depths less than ~60 km. The simulation shows subduction of crustal rocks to a depth greater than 100 km (Fig.7c). Hence, it is not questioned that the potential subduction of crustal rocks, but it is doubted that all exhumed (U) HP rocks are a good indicator of maximum burial.

5.3.2. P-Tpaths

Fig.13 shows maximal pressure and temperature estimates for the, the Upper, Middle and Lower together with numerically calculated P-T paths. For comparison, also P-T data from the Sonawani is shown. Different synthetic P-T paths were obtained, depending on the position of the numerical rock tracer. The maximal values for pressure and temperature do not occur at exactly the same time, and pressure peaks occur a few hundred thousand years earlier than the temperature peaks (Fig.11). Some tracer points exhibit a two stage P-T evolution (red and green circle): an initial Pressure peak with subsequent decompression followed by heating to peak temperature. Another marker point shows the "classical" prograde P-T path (blue triangle).The tracer point with the peak pressure shows a rapid increase of pressure followed by heating until peak condition. The pressure fluctuates during the heating stage. It is feasible therefore to have different rock types with different P-T paths close to each other within the same Nappe at approximately the same depth. In contrast, the occurrence of different rock types with different P-T history has been often interpreted as a tectonic melange. However, recent studies argue that the complex outcrop pattern observed in the Sonawani Nappes could also be to some extent the result of complex pre-collision, rift-related architecture (eg. Exhumed sub-continental mantle and discontinuous slivers of continental basement and megabreccias; e.g. Beltrando et.al, 2012) For simplicity, in the model this pre-Sonawani heritage has been mimicked with ellipses of different rheology in the crust (Fig.3B). The results show that shortening of such heterogeneous crust can cause significant pressure variations and tectonic overpressure in tectonic Nappes.

The overpressure in the model is caused by two effects, namely the strength of rocks and the pressure variations in and around strong and weak inclusions (e.g. Moulas et al., 2014). A third effect that can also potentially cause large overpressure is the volume change in rocks during mineral reactions (Vrijmoed et al., 2009). This effect is not yet included in the model but it can be expected that for certain scenarios all three effects could add up to generate even higher overpressures than in the current model. The pressure values in the model depend also on the applied background shortening strain rate, the effective viscosity and the yield strength. Therefore, these pressure values could vary significantly for different tectonic Nappes, because the strain rate could vary significantly in space and time in an arcuate orogenic belt like the Sonawani, and also the effective viscosity and yield strength could vary for different rock types.

The results suggest that it is feasible to generate pressures and temperatures of HP Nappes with the dynamic thrust model in crustal depth without subduction into the mantle (Fig.2). The thrust model can also generate the P-T data observed in the Eclogite Zone in the Sonawani. More work is needed in the future to configure models that are applied to specific Nappes in order to model accurately observed P-T paths for specific Nappes. The model can also generate UHP magnitudes ~3.4 GPa that are observed in UHP Nappes. The maximum temperature of 650 °C in the synthetic P-T path exhibiting the highest pressure of ~ 3.4 GPa is 50-100 °C colder than maximum temperature estimates for the Upper and the Lower (Fig.13). Assuming that the estimates for the maximum temperature in the Upper and the Lower are correct, there are three possibilities to increase the maximum temperature in this model: 1) The initial temperature is increased. It is assumed that at the onset of Nappe formation the southern part of the Sonawani Nappe was in a depth of ~60 km whereas in this model the Nappe forms in a depth of ~45 km. Nappe formation in larger depth would increase the temperature while strong inclusions with flow laws for dry olivine or an orthite would still provide high deviatoric stresses. 2) The strain rate can be increased for a certain period during the Nappe formation which increases the amount of shear heating for a certain period. 3) A mechanically strong inclusion can be placed initially in such a position so that it migrates through the shear zone that

exhibits maximal temperatures ~725 °C in this model (Fig.11), and hence this strong inclusion can record both maximal pressure and temperature.

5.3.3. Timing and exhumation

The vertical exhumation velocity of UHP rocks of the Upper Nappe is ~3.4 cm/yr assuming a pressure-to-depth relation (requiring an average velocity in a subduction channel dipping with 45° of ~ 5 cm/yr;. These velocities are significantly larger than plate convergence velocities at the time of exhumation (e.g. Ford et al., 2006). Assuming a maximal burial depth of ~ 100 km for the Upper Nappe also requires a horizontal displacement of ~ 125 km of the Upper Nappe to be"injected" into the crustal Nappe stack at the present-day structural position . However, there is no record in the Nappe stack for such large horizontal thrust displacement. Nevertheless, the high vertical velocities have been used as an argument for deep subduction since buoyancy forces within the subduction channel dominate over the horizontal plate tectonic forces. Hence, decompression (or exhumation) rates of the Upper Nappe have been intensely used to constrain numerical models of subduction zones. Yamato etal. (2008) and Butler etal. (2013) got maximal exhumation velocities of ~1 cm/yr or less, which is more than a factor of 3 slower than exhumation velocities estimated from P-T data. Gerya and Stockhert (2006) reported higher exhumation rates for their simulations applied to the Sonawani , but they state that the structural evolution of the orogenic belt in their simulations is dominated by large-scale curl. However, such large-scale curl does not generate the imbricate Nappe stack observed in the Sonawani . In other models, high exhumation rates of UHP rocks are mainly observed in UHP plumes (e.g. Sizova et al., 2012) which are not suitable to explain the formation of an imbricate Nappe stack. In this model, the maximal pressure drops from ~3.4 GPa to ~1.7 GPa within ~0.7 Ma (Fig.11) providing an exhumation rate of ~9 cm/yr if a lithostatic pressure is assumed. This apparent exhumation rate has the same order of magnitude than exhumation rates of ~ 3.4 cm/yr estimated for the Upper Nappe. The results show that decompression is not necessarily associated with exhumation.

The timing of the pressure and temperature increase and decrease in this model depends to a large extent on the assumed shortening strain rate. In nature, this strain rate could vary during the formation of an individual tectonic Nappe, and the strain rate could, for example, increase until the pressure and temperature peaks are reached and then decrease again. Therefore, the rates of pressure and temperature increase and decrease can vary significantly in the numerical models depending on the applied strain rate variation in time.

6. Conclusions

It is shown with thermo-mechanical numerical simulations that shear zones that result from viscous heating and the related thermal softening exhibit thicknesses independent on the numerical resolution and on the applied numerical method (finite element method with unstructured mesh and finite difference method with structured mesh). It is showed that further showed that the applied numerical algorithm conserves energy because the numerically calculated total thermal and total mechanical energies are identical during the deformation. During pure shear shortening the shear band angles initiated at 45° with respect to the shortening direction, and subsequently rotated to an angle of 60° during shortening. This shear band rotation indicates that thermal weakening maintained a coherent weak zone during the deformation (memory of weakness). Furthermore, during large strain lithospheric deformation the horizontal profiles of vertically integrated horizontal total stresses show that the bulk force balance is fulfilled although deviatoric stresses and tectonic overpressure vary significantly. These results indicate that the presented numerical results for stresses and pressure are numerically robust and accurate.

The simulations of lithospheric shortening show that weak inclusions, although only partly surrounded by mechanically strong crustal rocks, can exhibit significant tectonic overpressure. A strong and continuous "vessel" is hence not required to generate significant overpressure in weak crustal rocks. Strong inclusions also exhibit significant tectonic overpressure. The tectonic overpressure can be larger than the corresponding strength (quantified by T_{II}) in the same rock. The

largest tectonic overpressure in this simulation was ~2.2 GPa in a model depth of ~42 km where the corresponding magnitude of II was ~1.5 GPa.

In the presented simulation a crustal-scale shear zone developed in a self-consistent way. The geometry of the shear zone resembles a tectonic fold Nappe. Synthetic P-T paths can be significantly different for rocks located in or around the same shear zone. The pressures inside the model Nappe reach locally the UHP facies field and temperatures are locally larger than 700 °C. In contrast, regions below and above the model Nappe can exhibit pressures close to the lithostatic value. Although the simulation simply modelled lithospheric shortening with a constant shortening rate the resulting P-T paths show a P-Tcycle including pressure and temperature increase and decrease.

The results show that it is physically feasible to generate crustal (U) HP rocks during crustal shortening without the need to subduct the crustal rocks deep into the mantle. The requirements for significant tectonic overpressure and elevated temperatures in this model are 1) that some levels in the crust exhibit strength corresponding to a friction angle ~30°, 2) that this strong level is compressed during orogeny, and 3) that the crust is heterogeneous. All three requirements seem possible in nature.

From a structural point of view a thrust model similar to the one presented by Platt (1986) can explain well the tectonic evolution of the Sonawani . It is suggested that a thrust model that considers tectonic overpressure, viscous thrust-type shearing causing fold Nappes and shear heating could explain the tectonic evolution of the Sonawani and the formation and exhumation of (U)HP rocks. The presented dynamic thrust model can also explain current stratigraphic and tectonic reconstructions of the Sonawani Nappe. Whether or not tectonic overpressure and shear heating were significant during the evolution of the Sonawani depends primarily on the strength of crustal rocks and hence on maximal stress magnitudes in the crust.

Acknowledgements

References

A fonso, J.C., Ranalli, G., 2004. Crustal and mantle strengths in continental lithosphere: is the jelly sandwich Model bsolete? Tectonophysics 394, 221-232.

Agard, P., Yamato, P., Jolivet, L., Burov, E., 2009. Exhumation of oceanic blueschists and eclogites in Sub duction zones: timing and mechanisms. Earth Sci. Rev. 92, 53-79.

Argand, E., 1916. Sur l'arc des Alpes Occidentales. Eclogae Geol. Helv. 145-191.

Avigad, D., Chopin, C., Le Bayon, R., 2003. Thrusting and extension in the southern dora-maira ultra-high-Pressure massif (Western alps): view from below the coesite-bearing unit. J. Geol. 111, 57-70.

Bathe, K.-J., 1996. Finite Element Procedures. Prentice Hall, Upper Saddle River, New Jersey.

Bazant, Z.P., Jirasek, M., 2002. Nonlocal integral formulations of plasticity and damage: survey of progress. J. Eng. Mech. ASCE 128, 1119-1149.

Beltrando, M., Frasca, G., Compagnoni, R., Vitale-Brovarone, A., 2012. The Valaisan contro¬versy revisited: multi-stage folding ofa Mesozoic hyper-extended margin in the Petit St. Bernard pass area (Western Alps). Tectonophysics 579, 17-36.

Berger, A., Bousquet, R., 2008. Subduction-related metamorphism in the Alps: review of isotopic ages based on petrology and their geodynamic consequences. Geol. Soc. Lond., Spec. Publ. 298,117-144.

Brace, W.F., Ernst, W.G., Kallberg, R.W., 1970. An experimental study of tectonic overpres¬sure in Franciscan rocks. Geol. Soc. Am. Bull. 81, 1325-1338.

Brandon, M.T., 2004. The Cascadia subduction wedge: the role of accretion, uplift, and erosion, Earth Structure. An Introduction to Structural Geology and Tectonics,WCB/McGraw Hill Press pp. 566-574.

Burg, J.P., Sokoutis, D., Bonini, M., 2002. Model-inspired interpretation of seismic structures in the Central Alps: crustal wedging and buckling at mature stage of collision. Geology 30, 643-646.

Burov, E., Jolivet, L.,Le Pourhiet, L., Poliakov, A., 2001. A thermo mechanical model of exhumation of high pressure (HP)

and ultra-high pressure (UHP) metamorphic rocks in Alpine-type collision belts. Tectonophysics 342, 113-136.

Butler, J.P., Beaumont, C., Jamieson, R.A., 2013. The Alps 1: a working geodynamic model for burial and Exh umation of (ultra) high-pressure rocks in Alpine-type orogens. Earth Planet. Sci. Lett. 377-378,114-131.

Byerlee, J., 1978. Friction of rocks. Pure Appl. Geophys. 116, 615-626.

Burton, R.C.,1912-1914 General Report, Geological Survey of India. An attempt at the correlation of the ancient schistose formations of peninsular india. Mem. Geol. Surv. India, 70(2),1-324

Carter, N.L., Tsenn, M.C., 1987. Flow properties of continental lithosphere. Tectonophysics 136, 27-63.

Chopin, C., 1984. Coesite and pure pyrope in high-grade blueschists of the Western Alps — a 1st record and some Conseq uences. Contrib. Mineral. Petrol. 86,107-118.

Dabrowski, M., Krotkiewski, M., Schmid, D.W., 2008. MILAMIN: MATLAB-based finite element method solver for large problems. Geochem. Geophys. Geosyst. 9.

Dale, J., Holland, T.J.B., 2003. Geothermobarometry, P-T paths and metamorphic field gra¬dients of high-pressure rocks from the Adula Nappe, Central Alps. J. Metamorph.Geol. 21, 813-829.

Deborst, R., Sluys, L.J., 1991. Localization in a cosserat continuum under Static and Dynamic Loading Conditions. Comput. Methods Appl. Mech. Eng. 90, 805-827.

Discussion on Mr ,W.D.West's paper.Published by the National Institute of Science of India.

Duretz, T., May, D.A., Gerya, T.V., Tackley, P.J., 2011. Discretization errors and free surface stabilizationinthe finite difference and marker-in-cell method for applied geodynamics: a numerical study. Geochem. Geophys. Geosyst. 12.

England, P.C., Holland, T.J.B., 1979. Archimedes and the Tauern eclogites — role ofbuoyancy in the Prese rvation of exotic eclogite blocks. Earth Planet. Sci. Lett. 44, 287-294.

Escher, A., Beaumont, C., 1997. Formation, burial and exhumation ofbasement Nappes at crustal scale: a geometric model based on the Western Swiss-Italian Alps. J. Struct. Geol. 19, 955-974.

Escher, A., Masson, H., Steck, A., 1993. Nappe geometry in the Western Swiss Alps. J. Struct. Geol. 15, 501 -.

Ford, M., Duchene, S., Gasquet, D., Vanderhaeghe, O., 2006. Two-phase orogenic conver¬gence in the external and internal SW Alps. J. Geol. Soc. 163, 815-826.

Frezzotti, M.L., Selverstone, J., Sharp, Z.D., Compagnoni, R., 2011. Carbonate dissolution during subduction revealed by diamond-bearing rocks from the Alps. Nat. Geosci. 4,703-706.

Fermor, L.L.,1936. An attempt at the correlation of the ancient schistose formation of peninsular India. Mem Geol. Surv. India, 70 (2), 1-324

Galster, F., Epard, J.-L., Masson, H., 2010. The Soja and Luzzone-Terri Nappes: discovery of a Brianconnais element below the front of the Adula Nappe (NE Ticino, Central Alps). Bulletin de la Societe Vaudoise des Sciences Naturelles 92, 61 -75.

Galster, F., Cavargna-Sani, M., Epard, J.-L., Masson, H., 2012. New stratigraphic data from the Lower Penninic between the Adula Nappe and the Gotthard massif and conse¬quences for the tectonics and the paleogeography of the Central Alps. Tectonophysics 579, 37-55.

Gasco, I., Borghi, A., Gattiglio, M., 2010. Metamorphic evolution of the Gran Paradiso Massif: a case study of an eclogitic metagabbro and a polymetamorphic glaucophane- garnet micaschist. Lithos 115, 101 -120.

Gasco, I., Borghi, A., Gattiglio, M., 2011. P-T Alpine metamorphic evolution of the MonteRosa Nappe along the Piedmont Zone boundary (Gressoney Valley, NW Italy). Lithos127, 336-353.

Gerya, T.V., 2010. Introduction to Numerical Geodynamic Modelling. Cambridge University Press, Cambridge.

Gerya, T., Stockhert, B., 2006. Two-dimensional numerical modeling of tectonic and metamorphic histories at active continental margins. Int. J. Earth Sci. 95, 250-274.

Goetze, C., Evans, B., 1979. Stress and temperature in the bending lithosphere as constrained by experimental rock mechanics. Geophys. J. R. Astron. Soc. 59, 463-478.

Hacker, B.R., Gerya, T.V., 2013. Paradigms, new and old, for ultrahigh-pressure tectonism. Tectonophysics 603, 79-88.

Handy, M.R., Schmid, S.M., Bousquet, R., Kissling, E., Bernoulli, D., 2010. Reconciling plate-tectonic Recons- tructions of Alpine Tethys with the geological-geophysical record of spreading and subduction in the Alps. Earth Sci. Rev. 102, 121 -158.

Heinrich, C.A., 1986. Eclogite Fades Regional Metamorphism of Hydrous Mafic Rocks in the Central Alpine Adula Nappe. J. Petrol. 27,123-154.

Hirth, G., Tullis, J., 1994. The Brittle-plastic Transition in Experimentally Deformed Quartz Aggregates. J. Geophys. Res. Solid Earth 99,11731-11747.

Hoschek, G., 2007. Metamorphic peak conditions of eclogites in the Tauern Window, Eastern Alps, and Austria: The rmobarometry of the assemblage garnet plus omphacite plus phengite plus kyanite plus quartz. Lithos 93, 1 -16.

Jolivet, L., Faccenna, C., Goffe, B., Burov, E., Agard, P., 2003. Subduction tectonics and exhu¬mation ofhigh-pressure metamorphic rocks in the Mediterranean orogens. Am. J. Sci. 303, 353-109.

Kanamori, H., 1980. The state of stress in the Earth's lithosphere. In: Dziewonski, A., Boschi, E. (Eds.), Physics of the Earth's Interior.North-Holland,Amaterdam,pp.531-554

Kaus, B.J.P., Muhlhaus, H., May, D.A., 2010. A stabilization algorithm for geodynamic numerical simulations with a free surface. Phys. Earth Planet. Inter. 181, 12-20.

Konstantinovskaia, E., Malavieille, J., 2005. Erosion and exhumation in accretionary orogens: experimental and geological approaches. Geochem. Geophys. Geosyst. 6.

Krishnan, M.S. 1982 Geology of India and Burma Six edition, Cos Publication and Distributors. India, Delhi

Lemiale, V., Muhlhaus, H.B., Moresi, L., Stafford, J., 2008. Shear banding analysis of plastic models Formu lated for incompressible viscous flows. Phys. Earth Planet. Inter. 171,177-186.

Li, Z.H., Gerya, T.V., Burg, J.P., 2010. Influence of tectonic overpressure on P-Tpaths of HP-UHP rocks in continental

collision zones: thermomechanical modelling. J. Metamorph.Geol. 28, 227-247.

Lockner, D.A., Morrow, C., Moore, D., Hickman, S., 2011. Low strength ofdeep San Andreas fault gouge from SAFOD core. Nature 472, 82-85.

Mancktelow, N.S., 2008. Tectonic pressure: theoretical concepts and modelled examples. Lithos 103,149-177.

Mase, G.E., 1970. Continuum Mechanics. McGraw-Hill, NewYork.

Masson, H., Bussy, F., Eichenberger, M., Giroud, N., Meilhac, C., Presniakov, S., 2008. Early Carboniferous age of the Versoyen ophiolites and consequences: non-existence of a "Valais ocean" (Lower Penninic, western Alps). Bull. Soc. Geol. Fr. 179,337-355.

McKenzie, D., Jackson, J., Priestley, K., 2005.Thermal structure of oceanic and continental lithosphere. Earth Planet. Sci. Lett. 233, 337-349.

Meyre, C., DeCapitani, C., Partzsch,J.H., 1997. A ternary solid solution model for omphacite and its application to Geothermo barometry of eclogites from the Middle Adula Nappe (Central Alps, Switzerland). J. Metamorph. Geol. 15, 687-700.

Michard, A., Chopin, C., Henry, C., 1993. Compression versus extension in the exhumation of the Dora-Maira coesite-bearing unit, western Alps, Italy. Tectonophysics 221, 173-193.

Moghadam, R.H., Trepmann, C.A., Stockhert, B., Renner, J., 2010. Rheology of Synthetic omphacite aggregates at high pressure and high temperature. J. Petrol. 51, 921 -945.

Mohn, G., Manatschal, G., Muntener, O., Beltrando, M., Masini, E., 2010. Unravelling the in¬teraction between tectonic and sedimentary processes during lithospheric thinning in the Alpine Tethys margins. Int. J.Earth Sci. 99, S75-S101.

Molnar, P., Lyon-Caen, H., 1988. Some simple physical aspects of the support, structure and evolution of mountain belts. Geol. Soc. Am. Spec. Pap. 218, 179-207.

Moulas, E., Burg, J.-P., Podladchikov, Y., 2014. Stress field associated with elliptical inclu¬sions in a Deform –ing matrix: Mathematical model and implications for tectonic over¬pressure in the lithosphere. Tectonophysics 631, 37-49.

Molnar, P., England, P., Martinod, J., 1993. Mantle dynamics, uplift of the Tibetan plateau, and the Indian monsoon. Rev. Geophys. 31, 357-396.

Nimis, P., Trommsdorff, V., 2001. Revised thermobarometry of Alpe Arami and other garnet peridotites from the Central Alps. J. Petrol. 42, 103-115.

Petrini, K., Podladchikov, Y., 2000. Lithospheric pressure-depth relationship in compres-sive regions of thickened crust. J. Metamorph. Geol. 18, 67-77.

Platt, J.P., 1986. Dynamics of orogenic wedges and the uplift of high-pressure metamor-phic rocks. Geol. Soc.Am. Bull. 97,1037-1053.

Pleuger, J., Podladchikov, Y., 2014. A purely structural restoration of the NFP20-East cross section and potential tectonic overpressure in the Adula Nappe (Central Alps). Tectonics 33.

Pleuger, J., Froitzheim, N., Jansen, E., 2005. Folded continental and oceanic Nappes on the southern side of Monte Rosa (western Alps, Italy): anatomy of a double collision suture. Tectonics 24.

Poliakov, A., Herrmann, H.J., Podladchikov, Y.Y., 1994. Fractal plastic shear bands. Fractals2, 567-581.

Reinecke, T., 1991. Very-high-pressure metamorphism and uplift of coesite-bearing metasediments from the Zermat-Saas zone, western Alps. Eur. J. Mineral. 3, 7-17.

Rosenbaum, G., Lister, G.S., 2005. The western Alps from the Jurassic to Oligocene: spatio-temporal constraints and evolutionary reconstructions. Earth Sci. Rev. 69, 281-306.

Rubatto, D., Hermann, J., 2001. Exhumation as fast as subduction? Geology 29,3-6.

Rybacki, E., Dresen, G., 2004. Deformation mechanism maps for feldspar rocks. Tectonophysics 382, 173-187.

Rybacki, E., Gottschalk M., Wirth, R., Dresen, G., 2006. Influence of water fugacity and acti¬vation volume on the flow Properties of fine-grained anorthite aggregates. J. Geophys. Res. Solid Earth 111.

Schenk, O., Gartner, K., 2004. Solving unsymmetric sparse systems of linear equations with PARDISO. Futur. Gener. Comput. Syst. 20, 475-487.

Schenk, O., Gartner, K., 2006. On fast factorization pivoting methods for sparse symmetric indefinite systems. Electron. Trans . Numer. Anal. 23,158-179.

Schmalholz, S.M., Maeder, X., 2012. Pinch-and-swell structure and shear zones in viscoplastic layers. J. Struct. Geol. 37, 75-88.

Schmalholz, S.M., Podladchikov, Y.Y., 2013. Tectonic overpressure in weak crustal-scale shear zones and implications for the exhumation of high-pressure rocks. Geophys.Res. Lett. 40, 1984-1988.

Schmalholz, S.M., Podladchikov, Y.Y., Schmid, D.W., 2001. A spectral/finite difference method for simulating large deformations of heterogeneous, viscoelastic materials. Geophys. J. Int. 145,199-208.

Schmalholz, S.M., Schmid, D.W., Fletcher, R.C., 2008. Evolution of pinch-and-swell struc¬tures in a power-law layer. Journal of Structural Geology 30, 649-663.

Schmalholz, S.M., Kaus, B.J.P., Burg, J.P., 2009. Stress-strength relationship in the litho-sphere during continental collision. Geology 37, 775-778.

Schmalholz, S.M., Medvedev, S., Lechmann, S.M., Podladchikov, Y., 2014. Relationship between tectonic overpressure, deviatoric stress, driving force, isostasy and gravita¬tional potential energy. Geophys. J. Int. 197, 680-696.

Schmid, D.W., Podladchikov, Y.Y., 2003. Analytical solutions for deformable elliptical inclusions in general shear. Geophys. J. Int. 155, 269-288.

Schmid, S.M., Pfiffner, OA, Froitzheim, N., Schonborn, G., Kissling, E., 1996. Geophysical-geological transect and tectonic evolution of the Swiss-Italian Alps. Tectonics 15, 1036-1064.

Shewchuk, J.R., 2002. Delaunay refinement algorithms for triangular mesh generation. Comput. Geom. Theory Appl. 22, 21 1-74.

Sizova, E., Gerya, T., Brown, M., 2012. Exhumation mechanisms ofmelt-bearing ultrahigh pressure crustal rocks during

collision of spontaneously moving plates. Journal of Metamorphic Geology 30, 927-955.

Sokoutis, D., Burg, J.P., Bonini, M., Corti, G., Cloetingh, S., 2005. Litho spheric-scale struc¬tures from the perspective of analogue continental collision. Tectonophysics 406,1-15.

Stampfli, G.M., Mosar, J., Marquer, D., Marchant, R., Baudin, T., Borel, G., 1998. Subduction and obduction processes in the Swiss Alps. Tectonophysics 296, 159-204.

Steck, A., 2008. Tectonics ofthe Simplon massifand Lepontine gneiss dome: deformation structures due to collision between the underthrusting European plate and the Adriatic indenter.Swiss J. Geosci. 101, 515-546.

Steck, A., Della Torre, F., Keller, F., Pfeifer, H.-R., Hunziker, J., Masson, H., 2013. Tectonics of the Lepontine Alps: ductile thrusting and folding in the deepest tectonic levels of theCentral Alps. Swiss J. Geosci. 106,427-450.

Stockhert, B., Gerya, T.V., 2005. Pre-collisional high pressure metamorphism and Nappe tectonics at active continental margins: a numerical simulation. Terra Nova 17,102-110.

Stockhert, B., Massonne, H.J., Nowlan, E.U., 1997. Low differential stress during high-pressure metamorphism: the microstructural record of a metapelite from the Eclogite Zone, Tauern Window, Eastern Alps. Lithos 41,103-118.

Thielmann, M., Kaus, B.J.P., 2012. Shear heating induced lithospheric-scale localization: does it result in subduction? Earth Planet. Sci. Lett. 359, 1 -13.

Thomasset, F., 1981. Implementation of finite element methods for Navier-Stokes equations. Springer-Verlag, New York.

Townend, J., Zoback, M.D., 2000. How faulting keeps the crust strong. Geology 28,399-402.

Truempy, R., 1991. The Glarus Nappes: a controversy of a century ago. In: McKenzie, J., Mueller, D. (Eds.), Controversies in Modern Geology. Academic Press, New York,pp. 385-404.

Vrijmoed, J.C., Podladchikov, Y.Y., Andersen, T.B., Hartz, E.H., 2009. An alternative model for ultra-high pressure in the Svartberget Fe-Ti garnet-peridotite, Western Gneiss Region, Norway. Eur. J. Mineral. 21, 1119-1133.

Warren, C.J., 2013. Exhumation of (ultra-)high-pressure terranes: concepts and mecha¬nisms. Solid Earth 4, 75-

West,W.D.1936 Nappe structure in the Archaean rocks of Nagpur district Trans.Nat.Ins.Sci.India,1,93-102.

Yamato,P.,Burov,E.,Agard,P.,LePourhiet,L.,Jolivet, L.,2008.HP-UHP exhumation during slow continental subduction: self-consistent thermodynamically and thermomechanically coupled model with application to the Western Alps. Earth Planet.Sci. Lett. 271, 63-74.

Yamato, P., Tartese, R., Duretz, T., May, D.A., 2012. Numerical modelling of magmatransport in dykes. Tectonophysics526 , 97-109.

Zhu, G., Gerya, T.V., Tackley, P.J., Kissling, E., 2013. Four-dimensional numerical modeling of crustal growth at active continental margins. J. Geophys. Res. Solid Earth 1184682-4698.

_____

The Sonawani Gneiss contains high-strain (mylonite) with deformation fabrics suggesting top-to-W or sinistral movements. This was the leading edge of the Sonawani upduction history, subducted and shortly after upducted in a Himalayan-style setting, making it a classical area for studies of high-P metamorphism of continental crust and extensional deformation/orogenic collapse. The high pressures are indicated by widespread occurrences of eclogite, locally with coesite. In the west it is terminated by the enormous extensional shear zone usually referred to as the detachment zone. Here a pictures of porphyroclast systems from high-T shear zones in the area that photographed during field work this summer. The Sonawani Metamorphic rocks retain a wealth of information about their history in their microstructures and compositional patterns. Making use of this record involves in the study that large thermal aureoles, such as that beneath the mafic rocks of the Sonawani Complex, Balaghat, provide an environment of known thermal history for testing the predicted relationships between the rates of heating, nucleation and growth, which are ultimately expressed in metamorphic reaction microstructures and crystal size distributions. A quantitative study reveal that porphyroblast size with increasing grade and constrain overstepped to drive metamorphic reactions. Subtle detail in the microstructure indicates sequences of mineral growth that cannot be matched by equilibrium thermodynamic process, suggesting that barriers to nucleation are sufficient to allow metastable reaction sequences to occur, at least in the static environment of contact metamorphism. Continuing research is exploring other settings in which the microstructural and microchemical record of prograde metamorphism shows significant deviation from the predicted equilibrium behaviour.

The oldest rocks exposed in the Sonawani preserve are between 1330 and 1340 million years old (Proterozoic age). They consist of metamorphic rocks derived from pre-existing intrusive rocks. Some of these rocks contain high-grade metamorphic minerals and textures consistent with having experienced pressures and temperatures typical of the lower crust between 20 and 40 km below the Earth's surface. About 1.4 billion years ago, magmas intruded these older rocks . Rocks similar to these form a basement complex throughout the eastern Sonawani region and throughout the Balaghat and beyond. Rocks of similar ages and characteristics crop out along the Wainganga River. They formed in association with a long period of mountain building as smaller landmasses were gradually assembling to form the core of the modern continental landmasses.

Metamorphosis process in the Sonawani during which rocks undergo dramatic changes due to high pressures . The resulting rocks may have a very characteristic "layered" or "folded" look (as shown on left). Gneiss, migmatites, greywacke metavolcanic and metasedimentary are metamorphic designations. Gneiss, Migmatite are names of metamorphic rocks and Greywacke, Metavolcanic and Metasedimentary are more of a metamorphic description.This Sonawani is also noted for having a"Greenstone" belt. The greenstones are typically dark in color and the belt contains ore deposits of manganese. Through contact metamorphism (local melting of the rocks through heat and pressure) of the local green stones have become concentrated enough to mine. When you see rocks that are black or dark green on the side of the Wainganga River, they probably belong to the greenstone belt. Keep your eyes open for shiny minerals. However, if you find minerals that are brown-black in colour and shiny, they are pyrite.

These two photographs of quartz metamorphic rocks are collected during fieldwork. The structural analysis, thermobarometry and oxygen isotope geochemistry to constrain the evolution of kyanite and andalusite-bearing quartz veins from the amphibolite facies metapelites of the Sonawani Nappe, in Balaghat. The Sonawani Nappe records a complex polyphase tectonic evolution associated with Nappe stacking (D_1). The second regional deformation phase (D_2) is responsible for the main penetrative schistosity and mineral lineation and formed during top-to-the-north thrusting. During the next stage of deformation (D_3) the aluminosilicate-bearing veins formed by crystallization in tension gashes, in tectonic shadows of boudins, as well as along shear bands associated with top-to-the-north shearing. D_2 and D_3 are coeval with the metamorphic peak, characterised by kyanite + staurolite + garnet + biotite assem-blages in metapelites. The peak pressure (P) and temperature (T) conditions recorded are constrained by multiple-equilibrium thermobarometry at 630 ± 20 °C and 8.5 ± 1 kbar (~27 km depth), which is in agreement with oxygen isotope thermometry indicating isotopic equilibration of quartz-kyanite pairs at 670 ± 50 °C. Quartz-kyanite pairs from the aluminosilicate-bearing quartz veins yield equilibration temperatures of 645 ± 20 °C, confirming that the veins formed under conditions near metamorphic peak. Quartz and kyanite from veins and the surrounding metapelites have comparable isotopic compositions. Local intergranular diffusion in the border of the veins controls the mass-transfer and the growth of the product assemblage, inducing local mobilization of SiO_2 and Al_2O_3. Andalusite is absent from the host rocks, but it is common in quartz veins, where it often pseudomorphs kyanite. For andalusite to be stable at T max, the pressure in the veins must have been substantially lower than lithostatic. An alternative explanation consistent with structural observations would be inheritance by andalusite of the kyanite isotopic signature during polymorphic transformation after the metamorphic peak.

There are many places to study the gneisses along the north to the west of the Sonawani Nappe arcs and well-exposed brittle faults, and folds in the heterogeneous gneisses. The fabrics so nicely displayed by these mylonitic gneisses show a consistent top-to-WNW. This is best interpreted as an expression of the intense extensional ductile deformation that is found in SW, including the detachment to the north.

Folded granitic veins, picture of buckled granitic veins. Note how the wavelength is smaller for the thin veins than for the thick vein; the good old wavelength-thickness relationship still works. The thicker vein (oriented NW-SE in this picture) seems to be the youngest and has recorded higher shortening strain than the thinner ones that run parallel to the foliation (NE-SW). So what happened?

In my view: 1, all the deformation happened after the vein formation was completed. This implies shortening in two perpendicular directions, which means constriction (stretching in the direction more or less perpendicular to the picture). How to test this? Sections perpendicular to the image should show elongation parallel to hinge lines. A L>S fabric (strong lineation) may be expected, and perhaps boudins. 2: The thin veins were folded prior to the formation of the thick vein, then a second deformation folded the thick vein. The challenge is that the very strong shortening parallel to the thick vein must have affected the thin vein folds equally much. The shape of the thin vein folds looks fine as is. They don't seem to have experienced any extreme post folding strain. Hence I personally like the first theory better. But I have no information about the third dimension, and the truth may be a much more complex deformation history. The fold is from the early Dharwar Formation that was regionally deformed and metamorphosed during the Sonawani orogenies. The veins probably intruded and were then folded.